Space Sci Rev (2010) 154: 145–192
DOI 10.1007/s11214-010-9673-8

The Lunar Radar Sounder (LRS) Onboard the KAGUYA (SELENE) Spacecraft

T. Ono · A. Kumamoto · Y. Kasahara · Y. Yamaguchi · A. Yamaji · T. Kobayashi · S. Oshigami · H. Nakagawa · Y. Goto · K. Hashimoto · Y. Omura · T. Imachi · H. Matsumoto · H. Oya

Received: 10 September 2009 / Accepted: 29 June 2010 / Published online: 11 August 2010

Abstract The Lunar Radar Sounder (LRS) onboard the KAGUYA (SELENE) spacecraft has successfully performed radar sounder observations of the lunar subsurface structures and passive observations of natural radio and plasma waves from the lunar orbit. After the transfer of the spacecraft into the final lunar orbit and antenna deployment, the operation of LRS started on October 29, 2007. Through the operation until June 10, 2009, 2363 hours worth of radar sounder data and 8961 hours worth of natural radio and plasma wave data have been obtained. It was revealed through radar sounder observations that there are distinct reflectors at a depth of several hundred meters in the nearside maria, which are inferred to be buried regolith layers covered by a basalt layer with a thickness of several hundred meters. Radar sounder data were obtained not only in the nearside maria but also in other regions such as the farside highland region and polar region. LRS also performed passive observations of natural plasma waves associated with interaction processes between the solar wind plasma and the moon, and the natural waves from the Earth, the sun, and Jupiter. Natural

T. Ono · A. Kumamoto (✉) · H. Nakagawa · H. Oya
Tohoku University, Sendai 980-8578, Japan
e-mail: kumamoto@pparc.gp.tohoku.ac.jp

Y. Kasahara · Y. Goto · T. Imachi
Kanazawa University, Kakuma, Kanazawa 920-1192, Japan

Y. Yamaguchi · S. Oshigami
Nagoya University, Chikusa-ku, Nagoya 464-8601, Japan

A. Yamaji
Kyoto University, Sakyo-ku, Kyoto 606-8502, Japan

T. Kobayashi
Korea Institute of Geoscience & Mineral Resources, Yuseong-gu, Daejeon 305-350, Korea

K. Hashimoto · Y. Omura
Kyoto University, Gokasho, Uji 611-0011, Japan

H. Matsumoto
Kyoto University, Sakyo-ku, Kyoto 606-8501, Japan

radio waves such as auroral kilometric radiation (AKR) with interference patterns caused by the lunar surface reflections, and Jovian hectometric (HOM) emissions were detected. Intense electrostatic plasma waves around 20 kHz were almost always observed at local electron plasma frequency in the solar wind, and the electron density profile, including the lunar wake boundary, was derived along the spacecraft trajectory. Broadband noises below several kHz were frequently observed in the dayside and wake boundary of the moon and it was found that a portion of them consist of bipolar pulses. The datasets obtained by LRS will make contributions for studies on the lunar geology and physical processes of natural radio and plasma wave generation and propagation.

Keywords Lunar subsurface radar sounding · Lunar Radar Sounder (LRS) · KAGUYA (SELENE) spacecraft · Lunar mare layered deposits · Buried regolith · Auroral kilometric radiation (AKR) · Jovian hectometric (HOM) radiation · Lunar wake · Electrostatic solitary waves (ESW)

Abbreviations

1PPS	1 pulse per second
A/D	Analog-to-digital converter
AKR	Auroral kilometric radiation
ALSE	Apollo Lunar Sounder Experiment
BPF	Band-pass filter
CML	Jovian System III central meridian longitude
D/A	Digital-to-analog converter
DAM	Decametric radiation
DHU	Data handling unit
DSP	Digital signal processor
ECU	Electric control unit, which is a controller of the solar array paddle
EMC	Electromagnetic compatibility
ESW	Electrostatic solitary wave
FET	Field effect transistor
FFT mode	One of observation mode of the WFC-H; the spectrum data are produced by the onboard software using the Fast Fourier Transform
FIFO	First-in first-out memory
FMCW	Frequency modulated continuous wave
FPGA	Field programmable gate array
Ga	Giga years ago
GSE	Geocentric solar ecliptic coordinate system
HF	High frequency; frequency range from 3 to 30 MHz
HK	House keeping status
HOM	Hectometric radiation
HPF	High-pass filter
IF	Intermediate frequency
JAXA	Japan Aerospace Exploration Agency
LALT	Laser Altimeter onboard the KAGUYA spacecraft
LRS	Lunar Radar Sounder
LRS-A	LRS antenna units
LRS-E	LRS main electronics unit
LRS-P	LRS preamplifier units
LPF	Low-pass filter

MARSIS	Mars Advanced Radar for Subsurface and Ionospheric Sounding
MEX	Mars Express
MRO	Mars Reconnaissance Orbiter
NCO	Numerically controlled oscillator
NPW	Natural plasma wave receiver; a passive receiver of LRS covering from 20 kHz to 30 MHz
NPW-A	NPW low-rate waveform mode; operation mode of NPW subsystem
NPW-DS	NPW dynamic spectra mode; operation mode of NPW subsystem
NPW-PL	NPW polarization mode; operation mode of NPW subsystem
NPW-S	NPW spectra mode; operation mode of NPW subsystem
NPW-W	NPW waveform mode; operation mode of NPW subsystem
OBC	Onboard computer
PDC	Programmable down converter
PHASE mode	One of observation mode of the WFC-H; the intensity and phase difference between two orthogonal components at each frequency point are transported to the ground
PRF	Pulse repetition frequency
RF	Radio frequency
RGA	Reiner Gamma magnetic anomaly
RX1, RX2	Receiver 1, Receiver 2
SAR	Synthetic aperture radar
SDR	Sounder observation
SDR-A	SDR low-rate waveform mode; operation mode of SDR subsystem
SDR-W	SDR waveform mode; operation mode of SDR subsystem
SHARAD	Shallow Radar
SNR	Signal to noise ratio
SPLD	South Polar Layered Deposits
STEREO	Solar Terrestrial Relations Observatory
STP	Solar Terrestrial Physiscs
TC	Terrain Camera
TFG	Transfer frame generator
THR	Terrestrial hectometric radiation
TNR	Thermal noise receiver; a spectrum receiver onboard WIND spacecraft
TR	Transmitter/receiver switch
ULF	Ultra low frequency; frequency range from 300 Hz to 3 kHz
UT	Universal time
WAVE mode	One of observation mode of the WFC-H; the down-converted and decimated signals of in-phase and quadrature components are sent as telemetry data
WFC	Waveform capture; a passive receiver of LRS covering from 100 Hz to 1 MHz
WFC-DUMP	A special mode of WFC receiver, in which waveform is once stored in the onboard memory and sent to the ground later by a DUMP command
WFC-H	WFC-High; a fast sweep-frequency receiver covering from 1 kHz to 1 MHz
WFC-H-X	X component of WFC-H receiver; differential signal between LRS-A1 and LRS-A3 antennas is fed to the WFC-H receiver
WFC-H-Y	Y component of WFC-H receiver; differential signal between LRS-A2 and LRS-A4 antennas is fed to the WFC-H receiver

WFC-L	WFC-Low; a waveform receiver covering from 100 Hz to 100 kHz
WFC-L-X	X component of WFC-L receiver; differential signal between LRS-A1 and LRS-A3 antennas is fed to the WFC-L receiver
WFC-L-Y1	Y component of WFC-L receiver; differential signal between LRS-A2 and LRS-A4 antennas, or single signal from LRS-A2 antenna is fed to the WFC-L receiver
WFC-L-Y2	Single signal from LRS-A4 is fed to the WFC-L receiver
WFC-DSP	A digital board for WFC receiver

1 Introduction

KAGUYA was launched on September, 14, 2007 in order to explore the surface distribution of elements and minerals, surface and subsurface structures of the moon, the gravitational field, the magnetic field, and energetic particles originating from the moon, as well as from solar/interplanetary space (Kato et al. 2008). The Lunar Radar Sounder (LRS) is one of the scientific instruments onboard the KAGUYA main orbiter (Ono et al. 2008). The purposes of the LRS are (1) to perform the radar sounding of the lunar surface and subsurface structures in order to understand the evolution of the moon through an investigation of the stratigraphic and tectonic lunar subsurface features (Yamaji et al. 1998), (2) to observe natural plasma waves associated with interaction processes between the solar wind plasma and the moon, and (3) to observe the natural waves from the Earth, the sun, and Jupiter from the lunar orbit (see Fig. 1). The LRS consists of two orthogonal 30 m tip-to-tip antennas and three subsystems: the sounder observation (SDR), the natural plasma wave observation (NPW), and the waveform capture (WFC). A main objective of the SDR is to investigate the surface and subsurface structures of the moon using an HF radar technique, and the NPW and the WFC are passive receivers covering the frequency ranges from 20 kHz to 30 MHz, and from 100 Hz to 1 MHz, respectively.

The first lunar subsurface radar sounding was carried out by Apollo Lunar Sounder Experiment (ALSE) onboard the Command and Service Module of the Apollo 17 (Phillips et al. 1973; Porcello et al. 1974; Peeples et al. 1978; Sharpton and Head 1982; Cooper et al. 1994). The ALSE distinctly shows that radar sounding using HF range electromagnetic waves is a powerful method for exploring geological structures of planets and moons. Subsurface radar soundings of Mars were also performed by the Mars Advanced Radar for Subsurface and Ionospheric Sounding (MARSIS) onboard the Mars Express (MEX) (Picardi et al. 2005; Gurnett et al. 2005) and Shallow Radar (SHARAD) onboard the Mars Reconnaissance Orbiter (MRO) (Seu et al. 2004, 2007). Several new findings such as buried craters in the northern lowlands (Watters et al. 2006), and the thickness of South Polar Layered Deposits (SPLD) (Plaut et al. 2007; Milkovich and Plaut 2008; Milkovich et al. 2009) were returned by those Martian radar sounders.

The radar sounder system has also been applied for remote sensing of the topside ionosphere of the Earth since the 1960s by Alouette and ISIS spacecraft (Franklin and MacLean 1969; Jackson and Warren 1969). The spaceborne plasma sounder system has been improved through the Japanese sounding rocket missions such as K-9M-43, K-9M-49, K-9M-53, K-9M-56, L-3H-9, and S-310-28, and Japanese satellite missions such as Jikiken (EXOS-B) (Oya et al. 1981; Oya and Ono 1981, 1987), Ohzora (EXOS-C) (Oya et al. 1985; Obara and Oya 1985), Akebono (EXOS-D) (Oya et al. 1990) and Nozomi (Planet-B, unfortunately aborted in transfer orbit by spacecraft troubles) (Ono et al. 1998;

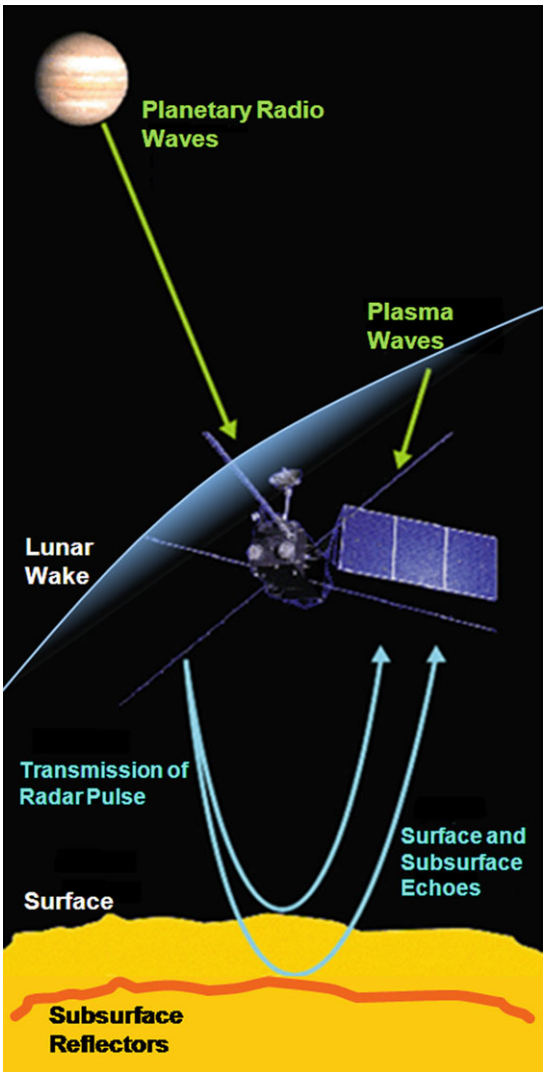

Fig. 1 A schematic picture of the purposes for the LRS observations

Oya and Ono 1998). Those plasma sounder systems have not been applied to the subsurface soundings of the planets and moons but could be applied to the solid targets.

The arrival time difference of the lunar surface and subsurface echoes at a depth of several km is typically several tens μsec, which is shorter than the sounder pulse width of the previous spaceborne plasma sounder systems. If the sounder pulse width is shortened to improve time resolution, the system signal-to-noise ratio (SNR) will be reduced. Range compression technique with Frequency Modulated Continuous Wave (FMCW) pulsing is one solution for detecting the lunar subsurface echoes with increased SNR. Time resolution of the FMCW radar is determined not by the pulse width but by band width of the pulse. We can thus use a sounder pulse with a long pulse width (or enough power) and obtain high-time (range) resolution data which is consistent with the required SNR. In addition, we are going to perform the Synthetic Aperture Radar (SAR) analysis (Kobayashi et al. 2002a, 2002b;

Kobayashi and Ono 2006, 2007). Azimuth compression of SAR analysis, which uses not single- but multiple-pulse data obtained along the spacecraft orbit considering the phase of echoes, will be effective for focusing on the subsurface echo signals.

Natural radio waves which are generated in space in a frequency range below 10 MHz are generally difficult to observe from the stations on the ground because they are reflected by the Earth's ionosphere. There are many spaceborne wave receivers which cover below 1 MHz. On the other hand, there are few spacecraft which cover above 1 MHz: for example, Akebono (Oya et al. 1990), WIND (Bougeret et al. 1995), Cassini (Gurnett et al. 2004), and STEREO (Bougeret et al. 2004). There are several natural wave phenomena such as terrestrial hectometric radiation (THR) (James et al. 1974; Oya et al. 1985; LaBelle et al. 1987), Type-III solar radio burst (Wild and McCready 1950; Wild et al. 1954), and Jovian hectometric (HOM) radiation (Carr and Desch 1976; Kaiser et al. 1979) in that frequency range. LRS is optimized to perform the lunar subsurface radar sounding in a frequency range from 4 MHz to 6 MHz (Ono and Oya 2000; Ono et al. 2008, 2009). Therefore, LRS can perform radio and plasma wave observations with high sensitivity in the frequency range covered by few spaceborne wave receivers.

The distance from the Earth to the moon is almost constant. LRS can perform stationary observations of the radio waves from the Earth. Not only the natural radio waves such as auroral kilometric radiation (AKR) (Gurnett et al. 1974) but also the artificial radio waves as measured by WIND (Kaiser et al. 1996) can be observed by LRS. The investigation of background noise level in the polar orbit will be useful for planning low-frequency radio astronomical telescopes on the moon or in the lunar orbit in the future (Lecacheux 1994; Bougeret 1996).

The WFC consists of two receivers, WFC-H and WFC-L. The WFC-H is a fast sweep frequency spectrum receiver covering the frequency range between 1 kHz up to 1 MHz while the WFC-L is a waveform receiver which covers the frequency range below 100 kHz. The lower frequency of the WFC-L is officially at 100 Hz but the filter is rolling up in frequency with a gentle slope, allowing the detection of lower frequency waveforms. By taking advantage of a moon orbiter, the WFC is expected to measure plasma waves related to solar wind-moon interaction, mini-magnetospheres caused by magnetic anomaly on the lunar surface, and radio emissions to be observed from the moon.

In order to achieve the objectives mentioned above, we developed the LRS. In the present paper, we review the scientific topics on LRS observations in Sect. 2. The designs of the subsystems and onboard software of the LRS system are described in Sect. 3. The operations of the LRS after the launch of the KAGUYA spacecraft are described in Sect. 4. Initial results of radar sounder observations as well as natural wave observations are shown in Sects. 5–7. The summary is given in Sect. 8.

2 Scientific Topics on LRS Observations

2.1 Scientific Topics on Lunar Subsurface Soundings

Apollo Lunar Sounder Experiment (ALSE), performed in the Apollo 17 mission, was the first subsurface radar sounding of the moon (Phillips et al. 1973). In ALSE HF1 operation, ALSE transmitted chirp pulses in a frequency sweep range from 5 MHz to 5.533 MHz. The range resolution of chirp radar is determined by $\Delta R = c/(2\Delta f)$, where Δf is frequency sweep range of the radar pulse. Because the frequency sweep range is 0.533 MHz, range

resolution of ALSE HF1 is $280/\sqrt{\varepsilon_r}$ m, where ε_r is the relative dielectric constant. Olhoeft and Strangway (1975) reported that the relative dielectric constant range of the lunar rock samples was from 1.6 to 11. The factor $1/\sqrt{\varepsilon_r}$ is, therefore, from 0.3 to 0.8. Peeples et al. (1978) reported, based on the ALSE HF1 (5 MHz) data, that there are two reflectors at depths of 0.9 km and 1.6 km in Mare Serenitatis and one reflector at a depth of 1.4 km in Mare Crisium. Because they estimated the dielectric constant of the surface media to be 8.7, the actual depth of the reflectors was expressed as $2.7/\sqrt{\varepsilon_r}$ km, $4.7/\sqrt{\varepsilon_r}$ km, and $4.1/\sqrt{\varepsilon_r}$ km. DeHon and Waskom (1976) estimated the thickness of mare basalts in Serenitatis and Crisium basins by using crater geometric techniques based on the relationship between crater diameter and rim height (Pike 1974). Their estimation suggests that basalt thickness in Maria Serenitatis and Crisium is larger than 1.5 km. Williams and Zuber (1998) used depth-diameter relation of not-buried craters determined by Clementine laser altimeter data and estimated mare basalt thickness. The estimated basalt thickness in Maria Serenitatis and Crisium were 4.30 km and 2.94 km. These estimations of mare basalt thickness were quite similar with the depth of reflectors observed by ALSE, assuming that $1/\sqrt{\varepsilon_r}$ is from 0.3 to 0.8. It is pointed out that there is a correspondence between thick basalts basins and mascons with large gravity anomaly. It is also suggested that the estimated mare basalt thickness, based on gravity anomaly, is much larger than those based on crater geometric techniques (Solomon and Head 1980).

KAGUYA/LRS was planned in order to perform subsurface radar sounding not only in the nearside maria around the equator, as performed by ALSE, but also on a wide area on the moon's surface. The KAGUYA is a polar orbiting spacecraft, which can scan the whole lunar surface within a half month with a longitudinal step of 1 degree. During the nominal 1-year operation, a global scan was performed 24 times. Therefore, the longitudinal resolution of observation was improved up to $1/24$ degree.

Surface structures such as mare ridges and grabens were formed by the processes associated with the thermal history of the moon. The thermal history model with an initial melting to 300-km depth and an initial cold interior was shown by Solomon and Head (1980). The model suggests that surface horizontal thermal stress changed from expansion, which made grabens, to contraction, which made ridges, at 3.6 billion years ago. Subsurface radar sounding can contribute to determine the formation processes and ages of ridges and grabens.

2.2 Scientific Topics Addressed by Wave Measurements Around the Moon

The scientific objectives of radio and plasma wave measurements roughly fall into two categories: (1) lunar science and (2) extra-lunar science. The former is the science of the plasma physics related to the moon itself. The latter is the science of the radio and plasma waves, originating from the Sun and the Earth and other planets, taking advantage of a moon orbiter.

2.2.1 Science on the Plasma Waves and Plasma Physics on the Moon

As was revealed by Explorer 35 and Apollo sub-satellites, the moon is known to be basically non-magnetized (e.g. Ness et al. 1968; Schubert and Lichtenstein 1974). Figure 2 is a schematic picture of the plasma environment around the moon when the moon is located in the solar wind. As the solar wind particles directly hit the lunar surface and are absorbed in the lunar body, a plasma cavity called the "lunar wake" is created behind the moon. In the next step, the solar wind acts to refill the wake region. The mechanisms of plasma expansion into the wake were studied by Samir et al. (1983). Because of the difference of thermal

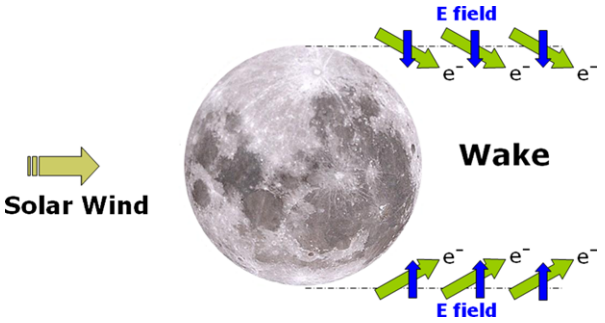

Fig. 2 A schematic picture of the plasma environment around the moon in the solar wind

speed between ions and electrons, electrons first attempt to refill the cavity, which causes an electric field at the boundary region of the wake and ions are assumed to be accelerated by the DC E-field. The wake boundary, therefore, could be a source region of plasma waves caused by this instability.

The WIND spacecraft traversed the lunar wake at a distance of 6.8 lunar radii (R_L) and observed particles and DC magnetic fields as well as plasma waves in the lunar wake. Kellogg et al. (1996) showed that the frequency of locally generated Langmuir waves fell to 4 kHz, which was the lower frequency limit of the Thermal Noise Receiver (TNR) (Bougeret et al. 1995) onboard WIND, because of the lunar wake vacuum and subsequent increase when the spacecraft emerges from the lunar wake. The frequency of the Langmuir wave fluctuated considerably, suggesting turbulence of the wake boundary. Furthermore, they reported two bands of waves in the lunar wake around 18 and 36 kHz which were suggested to be electromagnetic waves. They interpret that these waves propagated from outer regions of the lunar wake and these frequencies were at or near the plasma frequency outside the wake and its harmonic, respectively. They also suggest several kinds of plasma waves around the wake boundary such as whistler-mode waves and one which is not certainly identifiable with modes in uniform plasma.

Farrell et al. (1996) introduced ULF waves observed just prior to the lunar wake entry and they suggested that this ULF wave is a whistler-mode wave generated in the wake boundary caused by the electric field potential. Farrell et al. (1997) demonstrated that ion beams generated by an ambipolar electric field near the wake flanks are capable of generating broadband electrostatic noise that was observed in the frequency range of up to 6 kHz measured by WIND.

The plasma wave originated from the lunar wake was also identified by GEOTAIL spacecraft. Nakagawa et al. (2003) reported that left-handed, circularly polarized ULF waves with a frequency of 0.3–1.1 Hz were detected by GEOTAIL and they suggested that these waves were whistler-mode waves excited through the interaction with electron beams flowing in an anti-sunward direction downstream of the lunar wake and experienced a reversal of polarization in the solar wind frame of reference.

Compared with these past observations by WIND and GEOTAIL, KAGUYA turns around at an altitude of ∼100 km every 2 hours with an inclination of 90°, and we expect to clarify the spatial structure of the lunar wake as well as plasma dynamics around the wake.

Although the moon basically has a non-magnetized body, there are several magnetic anomalies on the lunar surface (Lin et al. 1998). According to the results from Lunar Prospector spacecraft, Lin et al. (1998) suggested that a kind of mini-magnetosphere might be constructed as a result of interaction between the solar wind and these magnetic anomalies. Kurata et al. (2005) studied a possibility of the presence of a mini-magnetosphere

over the Reiner Gamma magnetic anomaly (RGA) region on the moon. They estimated the vertical size of the mini-magnetosphere to be about 30 km or more. Kuncic and Cairns (2004) proposed a model for radio emissions associated with the mini-magnetosphere on the moon and predicted that f_p and $2f_p$ emissions are radiated in the foreshock region of a shock front associated with the mini-magnetosphere on the lunar surface. In addition to the measurements at a nominal altitude of 100 km, KAGUYA was descended to an altitude at 50 km and finally down to 10–30 km in order to investigate the magnetic anomalies and mini-magnetosphere on the lunar surface.

Another topic is the lunar ionosphere. The lunar ionosphere is known to be extremely tenuous compared with the Earth's ionosphere. The peak density is less than or equal to the solar wind density in theory. It was, nevertheless, reported that 500–1000 cm^{-3} electron densities were observed at altitudes of 5–10 km with a radio occultation technique from the Soviet Luna 19 and 22 in 1970s (Vyshlov and Savich 1979). This report is still controversial because the observed large density is difficult to explain theoretically without magnetic shielding from the solar wind. There must be unknown maintainable or transfer mechanisms of charged particles if such high dense plasma exists.

In the KAGUYA mission, measurements of an electron density profile above the lunar surface were also performed by the radio occultation technique using the spacecraft-Earth link of the OUNA (Vstar) sub-satellite (Imamura et al. 2008). As the radio occultation technique is an indirect method for measurement of an electron density profile on the lunar surface, it is necessary to take into account the effects of the Earth's ionosphere as a bias of the measurement quantity. On the other hand, we expect a direct measurement of in situ electron density by detecting the local plasma frequency by the WFC. We also plan to use another indirect measurement method using the propagation characteristics of AKR originating from the Earth (Goto et al. 2009). The principles of this method will be introduced in the section of "Initial Results".

2.2.2 Science on the Plasma and Radio Waves Propagating to the Moon

Taking advantage of a moon orbiter, it is expected to observe radio emissions such as Type III burst, AKR and some other plasma waves in the Earth's magnetosphere. We also expect to observe radio emissions from Jupiter. The NPW and WFC-H are designed to determine the precise phase difference between two orthogonal components of the wave, which is a very important clue in analyzing the wave characteristics. KAGUYA is also expected to clarify the features of plasma physics in the Earth's magnetosphere, making use of chances to measure plasma waves in the Earth's magnetosphere every month.

3 Instruments

With consideration of the purposes of LRS and science topics mentioned in the previous sections, the requirements for instrument design are summarized as follows: (1) LRS has functions for global subsurface radar soundings as performed by the ALSE. In order to ensure the detection of subsurface echoes from depths of several km, LRS uses the same operation frequency with that of ALSE. The transmission power and range resolution have to be higher than those of ALSE. (2) In order to detect the subsurface echoes from depths of several km, the noise level of the receiver should be lower than the background galactic noise level in the operation frequency range of the radar sounder. That is also needed for observations of planetary radio waves. (3) In order to perform comprehensive measurements of

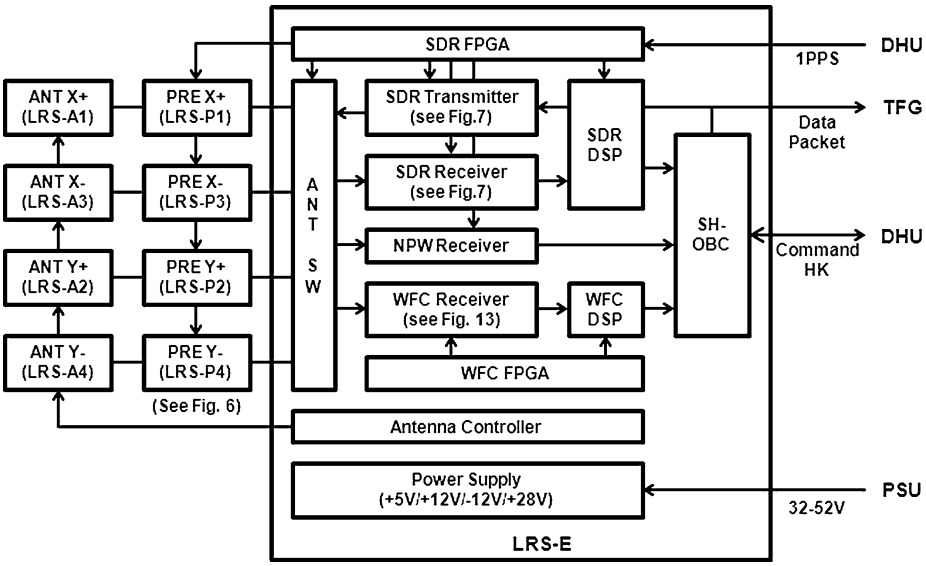

Fig. 3 Block diagram of LRS. LRS consists of 9 components: LRS-A1, A2, A3, A4 (Antenna units), LRS-P1, P2, P3, P4 (Preamplifier units), and LRS-E (Main electronics unit)

plasma dynamics related to the solar wind interaction with the moon in a micro-scale, waveform measurements as well as high-resolution spectrum measurements are indispensable. The LRS was designed based on the above requirements.

Figure 3 shows a block diagram of LRS. LRS consists of nine components: four antenna units (LRS-A1, A2, A3, and A4), four preamplifier units (LRS-P1, P2, P3, and P4), and a main electronics unit (LRS-E). All components are installed on the inner side of the +Z panel of the KAGUYA spacecraft. The instruments' parameters described below are summarized in Table 1. Details of instrument design were also described by Ono and Oya (2000), Ono et al. (2008), and Kasahara et al. (2008).

3.1 Antenna Units (LRS-A)

The LRS-A units are antenna elements with deployment mechanisms, which are utilized for transmission of radar sounder pulses and detections of the radar sounder echoes, and natural radio and plasma waves. The antenna length should be determined to maximize the sensitivity of radar sounder observations in a frequency range around 5 MHz. For the purpose of polarization measurements of natural radio and plasma waves, a cross dipole antenna is needed.

Four antennas, LRS-A1, A2, A3, and A4, are installed near the four corners of +Z panel of the KAGUYA spacecraft as shown in Figs. 4 and 5. After the deployment, the antennas form a cross dipole antenna, which enables polarization measurements of natural radio and plasma waves. The tip-to-tip length of each dipole antenna is 30 m. The sensitivity of the sounder is maximized at an operation frequency around 5 MHz. By attitude control of the spacecraft, the antenna plane is kept directed at the moon's center.

Because the KAGUYA spacecraft is not a spin-stabilized spacecraft, wire antenna systems cannot be used. Therefore, a rigid antenna system provided by TRW Astro Aerospace

Table 1 Instrument parameters of LRS

Resource requirements	
Mass	14.24 kg (LRS-E)
	1.080 kg (Total mass of four LRS-P units)
	7.784 kg (Total mass of four LRS-A units)
Power Consumption	56.7 W (Sounder observation)
	45.8 W (Passive observation)
Antenna	
Type	Cross dipole antenna
Tip-to-tip length	30 m
Material of antenna elements	BeCu alloy
Diameter of antenna elements	12.5 mm
Sounder observation	
Operation frequency	4–6 MHz (Nominal)
	14–16 MHz and 1 MHz (Option)
TX pulse width	200 μsec
Pulse Repetition Frequency (RPF)	20 Hz (SDR-W)
	2.5 Hz (SDR-A)
Sweep rate	10 kHz/μsec
Range resolution	75 m
TX power output	800 W
Sampling accuracy	12 bits
Sampling rate	6.25 MSPS
Sampling time	328 μsec (2048 points)
Dynamic range	from −90 dBm to −20 dBm (Gain-M)
Output data format	IF waveform (SDR-W, SDR-A)
NPW observation by SDR receiver	
Number of output channel	1 (E_X)
Frequency range	20 kHz–10 MHz
Sampling accuracy	12 bits
Sampling rate	25 MSPS
Sampling time	164 μsec (4096 points)
Sampling interval	100 msec
Frequency resolution	6 kHz
Dynamic range	from −186 to −111 dBV/m $Hz^{1/2}$ (Gain-H)
Output data format	RF waveform (NPW-W, NPW-A)
	Spectrum (NPW-S)
NPW observation by NPW receiver	
Number of output channels	2 (E_X and E_Y, or E_{LH} and E_{RH})
Frequency range	20 kHz–30 MHz
Frequency step	512 steps
Sweep time	2 sec
Band width	3 kHz (20 kHz–6 MHz)
	10 kHz (6 MHz–30 MHz)
Sampling accuracy	12 bits
Dynamic range	from −183 to −123 dBV/m $Hz^{1/2}$ (Gain-H)
Output data format	Spectrum (NPW-DS, NPW-PL)

Table 1 (*Continued*)

WFC observation	
Number of output channels	2 (E_X and E_Y) or 3 (E_X, E_{Y+}, and E_{Y-})
Frequency range	1 kHz–1 MHz (WFC-H)
	100 Hz–100 kHz (WFC-L)
Sweep time	0.5 sec
Sampling accuracy	16 bits
Dynamic range	from −10 dbμV to 106 dbμV
Output data format	Spectrum (WFC-H), RF Waveform (WFC-L)

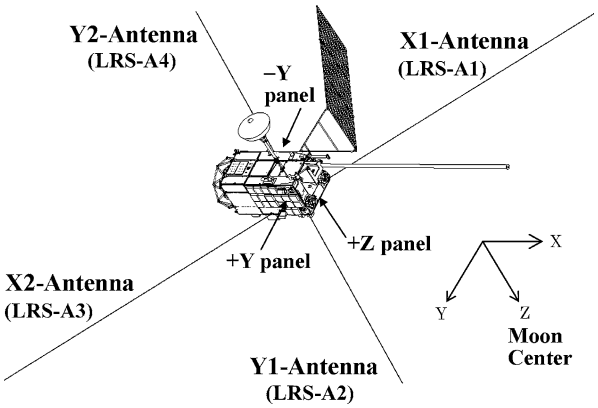

Fig. 4 Directions of LRS antenna with respect to the spacecraft body. All antenna elements are deployed in a plane parallel to the +Z Panel of the spacecraft. The +Z panel always faces the moon by attitude control of the spacecraft. The antenna plane is, therefore, always directed toward the moon

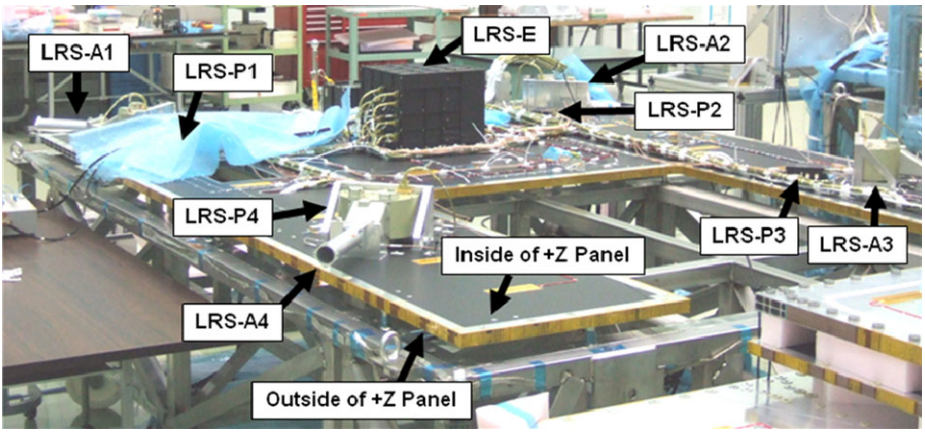

Fig. 5 Subcomponents of LRS in the first interface test of the spacecraft in Tsukuba Space Center (TKSC). All components are installed inside the +Z panel of the spacecraft

(Northrup-Grumann Astro Aerospace) was utilized for the KAGUYA spacecraft. The antenna element of LRS-A is rigid with cylindrical structures made of BeCu alloy, with a length of 15 m, a diameter of 12.5 mm, and a thickness of 51 μm. The antenna capacitance is therefore calculated to be 61 pF.

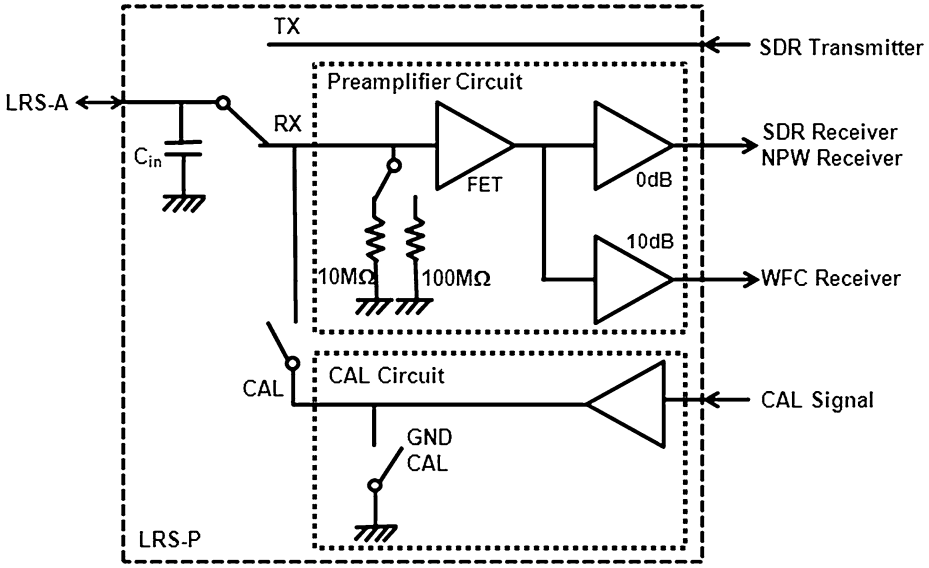

Fig. 6 Block diagram of LRS-P unit. LRS-P unit contains preamplifier circuit for signal from antenna unit, circuits for calibration and relays for switching between transmitter and receiver

3.2 Preamplifier Units (LRS-P)

The LRS-P units are preamplifiers for amplifying and buffering weak signals of radar sounder echoes, and natural radio and plasma waves detected by LRS-A units. The LRS-P1, P2, P3, and P4 units are installed directly adjacent to the corresponding antenna units, LRS-A1, A2, A3, and A4, respectively. Each LRS-P unit contains a preamplifier circuit for amplifying the signals from the antenna unit, circuits for calibration and relays for switching between transmitter and receiver as shown in Fig. 6.

When LRS-A1 and A3 are used as transmission antennas, signal lines to LRS-A1 and A3 are connected to the sounder transmitter subsystem in LRS-E unit. When LRS-A1 and A3 are used as receiving antennas, signal lines from LRS-A1 and A3 are connected to preamplifier circuits in LRS-P1 and P3 units. The preamplifier circuit consists of a front-end FET with high-input impedance and an amplifier for the SDR, NPW, and WFC receivers. The preamplifier circuit acts as an amplifier with a gain of 10 dB for the SDR and NPW receivers, and a buffer with unity gain for the WFC receiver. The input impedance of the front end buffer is selectable between 100 MΩ and 10 MΩ depending on operation modes. The input capacitance measured in prelaunch calibration was 16 pF.

3.3 Main Electronics Unit (LRS-E)

The LRS-E unit is the main electronics unit used for performing the generation of radar sounder pulses, amplification and signal processing of radar sounder echoes, and natural radio and plasma waves detected by dipole antennas. The LRS-E consists of the following subsystems: (1) SDR (Sounder) transmitter, (2) SDR receiver, (3) NPW (Natural Plasma Wave) receiver, (4) WFC (waveform capture) receiver, (5) antenna deployment controller, and (6) power supply.

3.3.1 SDR Transmitter

A block diagram of the SDR transmitter is shown in Fig. 7. The sounder transmitter is designed to perform the FMCW radar observations mainly in a frequency range of 4–6 MHz. LRS is also designed to perform sounder observations in 14–16 MHz, and at 1 MHz, as an option. However, most operations are performed in a frequency range of 4–6 MHz. The frequency range around 5 MHz was selected by following the ALSE. The frequency sweep range of LRS is, however, larger than that of ALSE. The range resolution of LRS is therefore $75/\sqrt{\varepsilon_r}$ m, which is improved from that of ALSE, or $280/\sqrt{\varepsilon_r}$ m. The source signals of the radar sounder pulse are generated by a digital-to-analog (D/A) converter with a sampling rate of 50 MHz. Before starting the radar sounder observation, the waveform of the radar sounder pulse is calculated by a digital signal processor (DSP) and stored in the memory which can be accessed also from the D/A converter. The waveform data of the source signal is expressed as follows:

$$V_{TX}(t) = V_0 \sin\left(\pi \frac{t - \tau_{TX}}{T}\right) \sin\left(\int_{\tau_{TX}}^{t} 2\pi \left(f_0 + f \cdot \left(t' - \tau_{TX}\right)\right) dt'\right) \tag{1}$$

where t is time, τ_{TX} is the starting time of the sounder pulse transmission, $T = 200$ μsec is the sounder pulse width, V_0 is the maximum amplitude of the sounder pulse, $f_0 = 4$ MHz is the starting frequency of the sounder pulse, and $\dot{f} = 2$ MHz/200 μsec is the frequency sweep rate of the sounder pulse. In order to reduce the spurious noise in the frequency spectrum of the sounder pulse, a sine-shape envelope is applied to the amplitude of the sounder pulse. Digital waveform data for generating source signals of sounder pulses by D/A converter are shown in Fig. 8. The source signals are fed into a power amplifier system which consists of 4 units, each unit containing a transformer-coupled class-AB push-pull amplifier operated by a power source with a voltage of 45 V as shown in Fig. 9(a). The 4-power amplifier units work in parallel with push-pull operation for achieving the transmission power of 800 W, as shown in Fig. 9(b). In order to transmit a sounder pulse with a power of 800 W, the power amplifiers are designed to have an efficiency of 25%, and a current of 70 A should be provided to the power amplifier for 200 μsec, or a pulse width. The energy can be provided with enough margins by the capacitor bank with a capacitance of 8000 μF. The waveform of the power amplifier output with 50 Ω load impedance is shown in Fig. 10.

In order to perform transmission and receiving with the same antenna, a transmitter/receiver (TR) switch (Franklin and MacLean 1969), as shown in Fig. 11, was built into the radar sounder system of LRS. A gate pulse, with a voltage of −300 V, is sent to the TR switch 25 μsec before the power amplifier transmits the sounder pulse. The SDR receiver is, then, disconnected from the antenna by reverse biased diodes. The gate pulse is terminated at 25 μsec after the transmission of the sounder pulse. The SDR receiver is connected again by forward biased diodes. In order to protect the receiver from the high-voltage radio frequency (RF) signals produced by the power amplifier (up to 1000 $V_{p\text{-}p}$), the switching diode must have a high break down voltage with high resistance and low capacitance in the reverse biased condition. In addition, in order to reduce insert loss of the TR switch, bias current for each diode should be large enough (several mA) while avoiding magnetic saturation of the transformer. Therefore, switching diode UM7010B and transformer FPQ3220 with 2500B material were utilized in the TR switch. The insertion loss of the TR switch measured in preflight calibration is 13 dB (Ono et al. 2008).

The timing of the sounder pulse transmission is controlled by the sequence controller which is shared with the SDR receiver. The timing chart used for sounder pulse transmis-

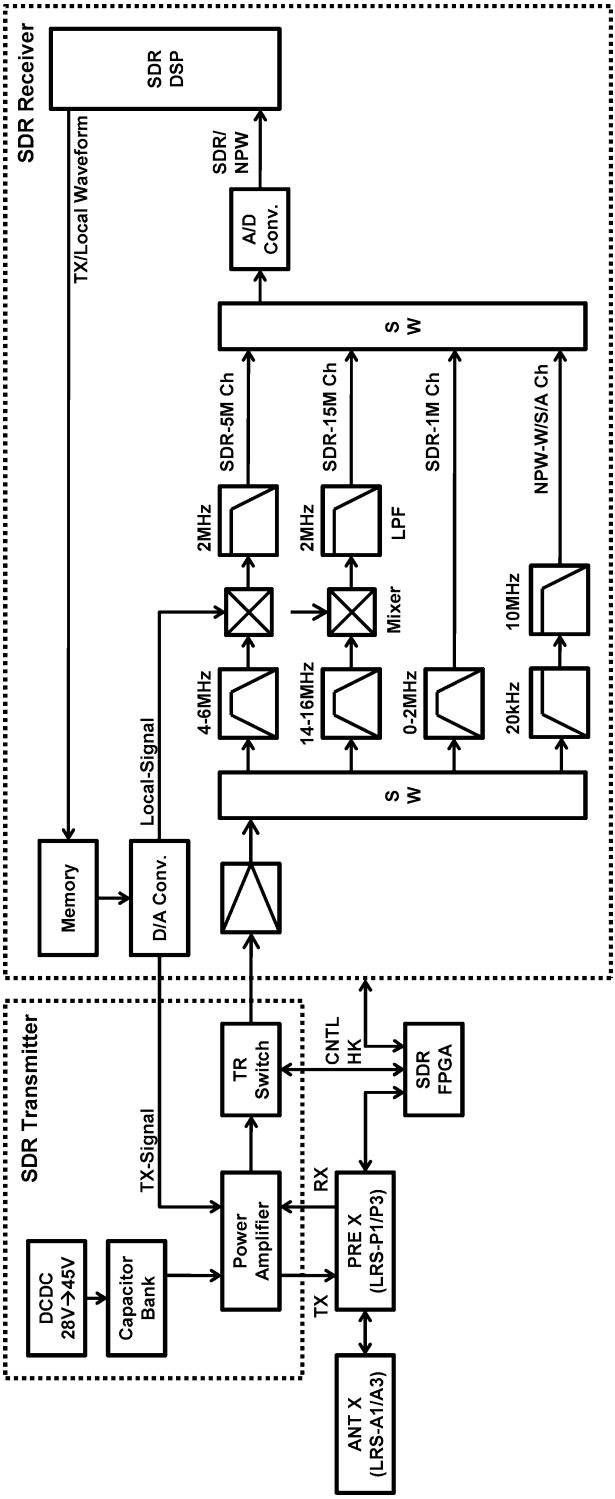

Fig. 7 Block diagram of SDR transmitter and receiver. SDR transmitter consists of power amplifier, TR switch, and capacitor bank. SDR receiver consists of RF amplifier, band-pass filters (BPF), mixer with local signal, and low-pass filters (LPF). D/A converter and memory are shared by sounder transmitter and receiver

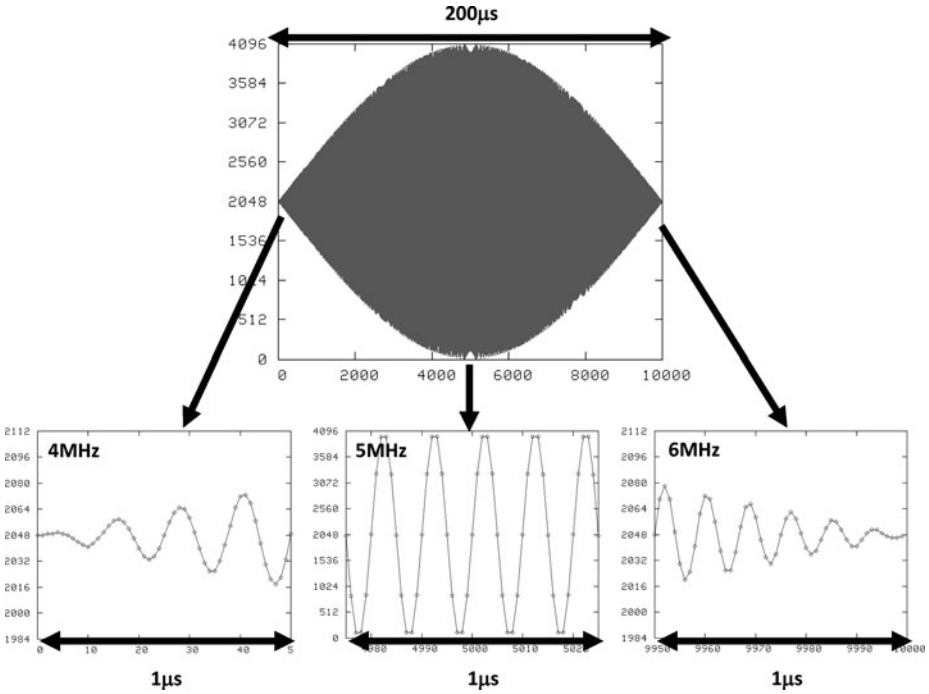

Fig. 8 Digital waveform data for generating source signal of the sounder pulse. The career frequency is swept from 4 MHz to 6 MHz within 200 μsec. In order to reduce the spurious noises in the frequency spectrum of the sounder pulse, sine-shape envelope is applied to the amplitude

sion is shown in Fig. 12. The sounder pulse transmission starts at 10 msec after the 1 pulse per second (1PPS) clock, which is provided by the data handling unit (DHU) of the spacecraft. After that, 20 sounder pulses are transmitted with an interval of 50 msec, or pulse repetition frequency (PRF) of 20 Hz. The width of the sounder pulse is 200 μsec. The guard pulse, which is sent to other observation instruments onboard the KAGUYA in order to notify the timing of the sounder pulse transmission, rises at 50 μsec before the sounder pulse transmission. The gate pulse for the TR switch and base bias of power transistor start to impress at 25 μsec and 12.5 μsec before the sounder pulse transmission, respectively. It can be confirmed in Fig. 10 that the RF pulse width is exactly 200 μsec without any trailing noises.

3.3.2 SDR (SDR/NPW-S/A/W) Receiver

The block diagram of the SDR receiver is shown in Fig. 7. There are four channels for sounder echoes with frequencies of 4–6 MHz, 14–16 MHz, and 1 MHz, and for natural radio and plasma waves in a frequency range from 20 kHz to 10 MHz. The four channels are enabled exclusively by analog switches. In a normal radar sounder operation, the channels for sounder echoes, with a frequency of 4–6 MHz, and for natural radio and plasma waves are utilized.

During sounder observations, the echo signals detected by LRS-A are sent to the SDR receiver via the TR switch of the sounder transmitter. The echo signal is amplified by an RF amplifier. The gain is selectable by the attenuator at the input of RF amplifier. After

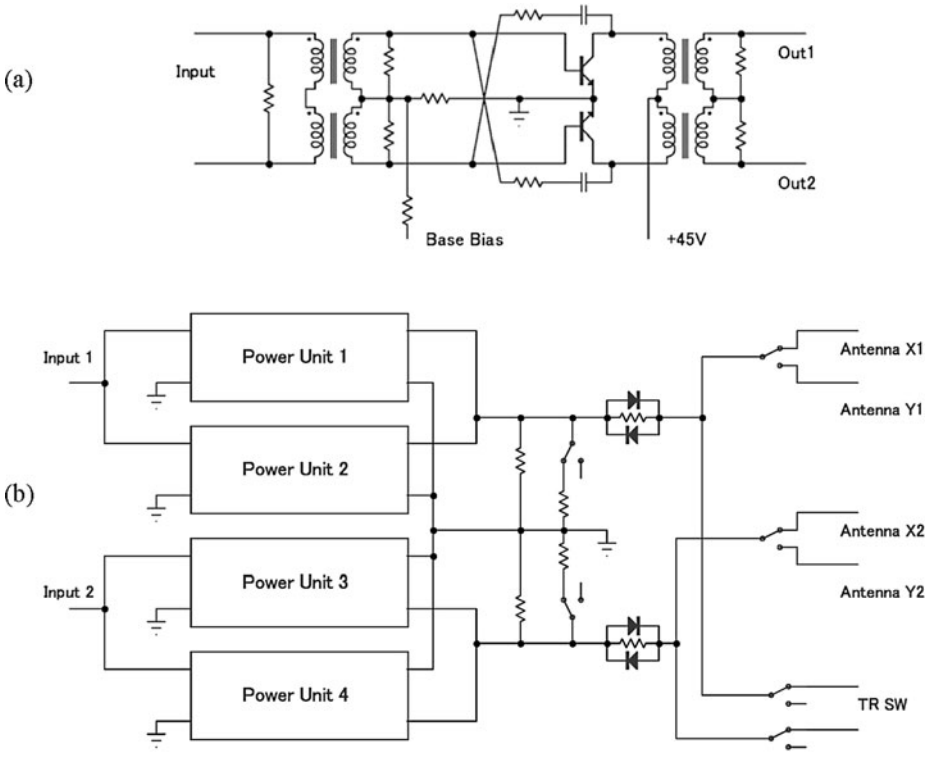

Fig. 9 (**a**) Circuit diagram of single power amplifier unit. (**b**) Block diagram of power amplifier system. Power amplifier system consists of 4 power amplifier units working in parallel with push-pull operation

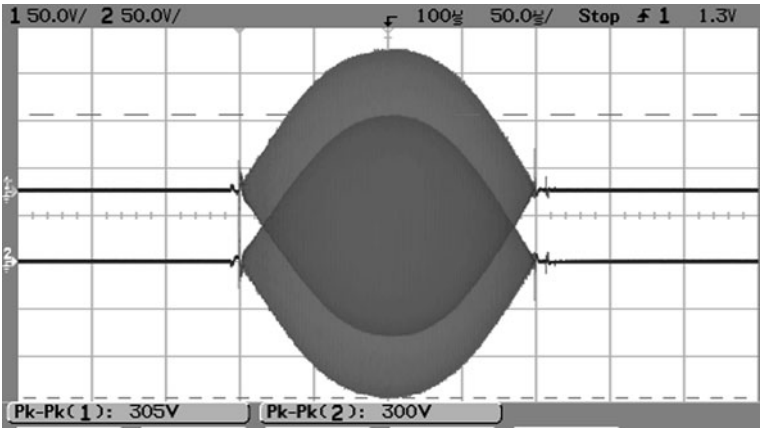

Fig. 10 An example of a waveform envelope of the power amplifier output for 50 Ω impedance load

the amplification by RF amplifier, the signals are mixed with local signals generated by a D/A converter. Before starting the radar sounder observation, the waveform data of the local signal is calculated by DSP and stored in the memory. The waveform data of the local signal

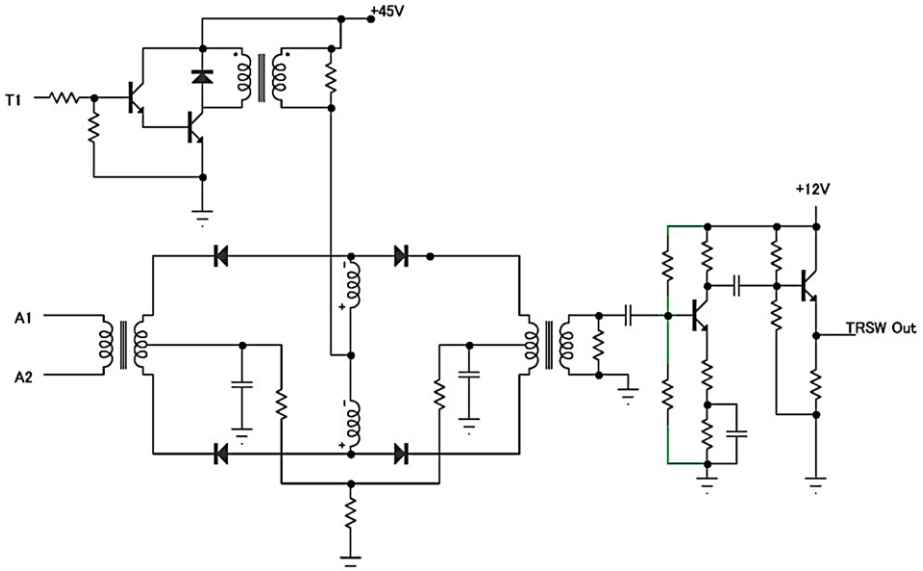

Fig. 11 Circuit diagram of TR switch. While the gate pulse with −300 V is impressed, the SDR receiver is disconnected from antenna elements with high voltage RF signal by reverse biased diodes

is expressed as follows:

$$V_{LO}(t) = V_0 \sin\left(\int_{\tau_{LO}}^{t} 2\pi \left(f_0 + \dot{f}\left(t' - \tau_{LO}\right)\right) dt'\right) \tag{2}$$

where τ_{LO} is start time of local signal mixing, and V_0 is the amplitude of local signal. Because the spacecraft altitude is about 100 km, the radar echo returns about 660 μsec after the radar transmission. The start time of the local signal is therefore set to around 660 μsec as shown in Fig. 12, which is changed depending on the predicted spacecraft altitude uploaded from the ground station. After the mixing of the local signal, the low-frequency component is selected by low-pass filter with a cut-off frequency of 2 MHz. The phase of intermediate frequency (IF) signal is given by

$$\begin{aligned}\phi &= \int_{\tau_{LO}}^{t} 2\pi \left(f_0 + \dot{f}\left(t' - \tau_{LO}\right)\right) dt' - \int_{\tau_{RX}}^{t} 2\pi \left(f_0 + \dot{f}\left(t' - \tau_{RX}\right)\right) dt' \\ &= 2\pi \left\{ \dot{f}\left(\tau_{RX} - \tau_{LO}\right)\left(t - \tau_{LO}\right) + f_0\left(\tau_{RX} - \tau_{LO}\right) - \frac{1}{2}\dot{f}\left(\tau_{RX} - \tau_{LO}\right)^2 \right\}\end{aligned} \tag{3}$$

where τ_{RX} is the arrival time of the echo signal. The IF waveform data are sent to the ground stations. We can then obtain $f_{IF} = \dot{f}(\tau_{RX} - \tau_{LO})$ by Fourier transform of the IF waveform data performed on the ground. We finally obtain ranges of echo reflectors by

$$R = \frac{c}{2\sqrt{\varepsilon_r}}\left(\tau_{RX} - \tau_{TX}\right) = \frac{c}{2\sqrt{\varepsilon_r}}\frac{f_{IF}}{\dot{f}} \tag{4}$$

where c is the speed of light, and ε_r is the relative dielectric constant of surface media. Thus chirp radar gives range of echo reflector not by arrival time of echo top but by frequency of

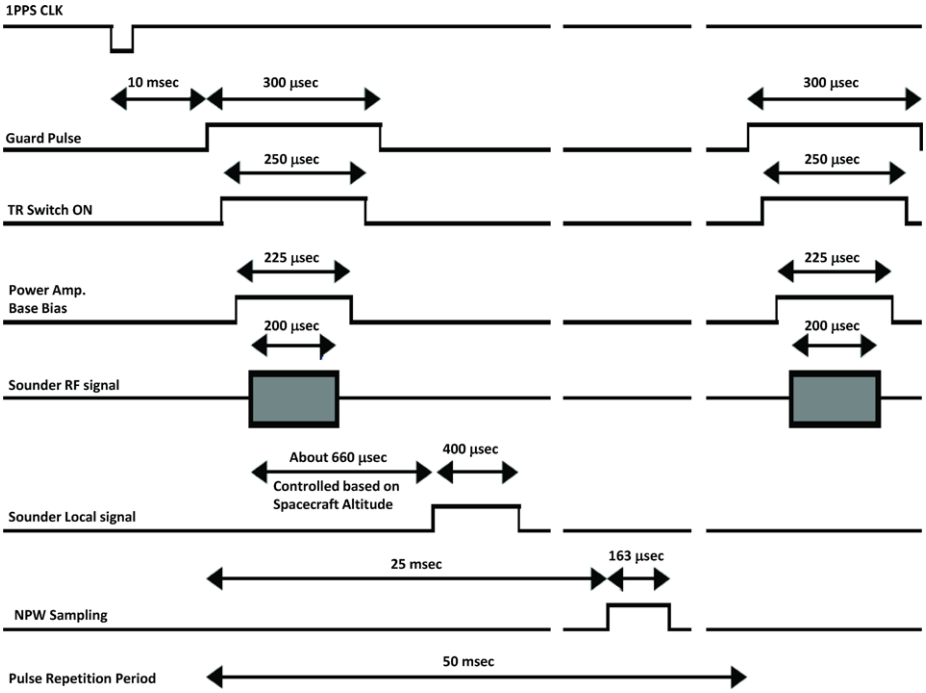

Fig. 12 Timing chart of sounder transmitter and receiver. The RF pulse is transmitted 10 msec after the 1PPS clock provided by spacecraft DHU. RF pulse width is 200 µsec. Guard pulse with a width of 300 µsec is sent to other observation instruments onboard the KAGUYA in order to notify the timing of the sounder pulse transmission

IF echo signal (range compression technique). It enables us to use temporally-spread radar pulse in order to improve SNR without degrading range resolution. By mixing these with reference functions derived from the expected variations of ϕ depending on the spacecraft locations, further SNR improvement can be achieved, which is called azimuth compression, or synthetic aperture radar (SAR) analysis. The IF signal is converted to the 2048 points of digital waveform data by 12 bit analog-to-digital (A/D) converter with a sampling frequency of 6.25 MHz. The dynamic range of the SDR receiver is therefore 72 dB. The start time of the A/D conversion is the same as the start time of the local signal. The dynamic range of the SDR receiver with medium gain is from -90 dBm to -20 dBm. We performed sounder observation with switching two operation modes, SDR-W and SDR-A (see Table 2), based on allowed telemetry rate for LRS. All waveform data with intervals of 50 msec are acquired in SDR-W mode while partial waveform data with intervals of 400 msec are acquired in SDR-A mode.

The SDR receiver is designed to perform not only the sounder observations but also the natural radio and plasma wave observations in a frequency range from 20 kHz to 10 MHz simultaneously. The natural radio and plasma waves detected by LRS-A are sent to the SDR receiver and sampled by an A/D converter. In order to obtain high-resolution sounder data within a limited telemetry rate, the NPW waveform data are converted to low-rate spectrum data (NPW-S mode, see Table 2) or low-rate waveform data (NPW-A mode, see Table 2) by onboard data processing.

Table 2 Operation mode of SDR, NPW, WFC subsystem

Subsystem	Operation Mode	Data Type and Rate	Frequency Range
SDR	SDR-W-XX/488 kbps	E_X Waveform/50 msec	4–6 MHz
	SDR-W-XY/488 kbps	E_Y Waveform/50 msec	(IF: 0–2 MHz)
	SDR-A-XX/80 kbps	E_X Waveform/400 msec	
NPW	NPW-W/488 kbps	E_X Waveform/0.1 sec	0.02–10 MHz
	NPW-A/16 kbps	E_X Waveform/4 sec	
	NPW-S/4 kbps	E_X Spectrum/8 sec	
	NPW-DS/16 kbps	E_X&E_Y Spectrum/2 sec	0.02–30 MHz
	NPW-PL/16 kbps	E_{LH}&E_{RH} Spectrum/2 sec	
	NPW-DS/2 kbps	E_X&E_Y Spectrum/16 sec	
	NPW-PL/2 kbps	E_{LH}&E_{RH} Spectrum/16 sec	
WFC	WFC-H&L/160 kbps	E_X&E_Y Spectrum/0.5 sec	1 kHz–1 MHz (H)
	WFC-H&L/80 kbps	E_Y Spectrum/0.5 sec	100 Hz–100 kHz (L)
	WFC-H/4 kbps	E_X&E_Y Spectrum/2 sec	
	WFC-H/2 kbps	E_X&E_Y Spectrum/4 sec	

The SDR receiver can be operated continuously as a passive waveform receiver for observation of natural radio and plasma waves in a frequency range from 20 kHz to 10 MHz (NPW-W mode, see Table 2). Dynamic range of the SDR receiver in NPW-W mode with high gain is from -110 dBm to -35 dBm, or from -186 dBV/m$\sqrt{\text{Hz}}$ to -111 dBV/m$\sqrt{\text{Hz}}$ around 5 MHz.

3.3.3 NPW (NPW-DS/PL) Receiver

The NPW receiver in the LRS-E unit is a sweep frequency analyzer for observation of natural radio and plasma waves in a frequency range from 20 kHz to 30 MHz while the sounder observation is suspended. It consists of two channels of the receiver named RX1 and RX2. The sweep time is 2 sec. The frequency table is shown in Table 3. It should be noted that frequency gaps are 16 kHz in Band 1 (0.020–2.068 MHz), 32 kHz in Band 2 (2.068–6.164 MHz), 64 kHz in Band 3 (6.164–14.356 MHz), and 128 kHz in Band 4 (14.356–30.612 MHz). The band width of RX1 and RX2 channels is 3 kHz in Bands 1 and 2 (0.020–6.146 MHz), and 10 kHz in Bands 3 and 4 (6.164–30.612 MHz). In normal observation, RX1 and RX2 are respectively used for measurements of X and Y components of natural radio and plasma waves (NPW-DS mode, see Table 2). In polarization observation, RX1 and RX2 are respectively used for measurements of left-handed and right-handed components of natural radio and plasma waves by connecting the hybrid-transformer bridge (NPW-PL mode, see Table 2). Dynamic range of NPW receiver with high gain is from -110 dBm to -50 dBm, or from -183 dBV/m$\sqrt{\text{Hz}}$ to -123 dBV/m$\sqrt{\text{Hz}}$ around 5 MHz.

3.3.4 WFC Receiver

WFC receiver is designed to measure natural radio and plasma waves in a frequency range from 10 Hz to 1 MHz. A block diagram of the WFC is shown in Fig. 13. The signals detected by LRS-A are passed through the LRS-P units, and fed into the WFC. The WFC consists of

Table 3 Frequency table of NPW receiver. Frequency range from 20 kHz to 30.612 MHz is covered by 512 frequency steps

Band	Freq. Step	RF [MHz]	Δf [kHz]	BW [kHz]
1	0	0.020	16	3
	1	0.036		
	:	:		
	127	2.052		
2	128	2.068	32	
	129	2.100		
	:	:		
	255	6.132		
3	256	6.164	64	10
	257	6.228		
	:	:		
	383	14.292		
4	384	14.356	128	
	385	14.484		
	:	:		
	511	30.612		

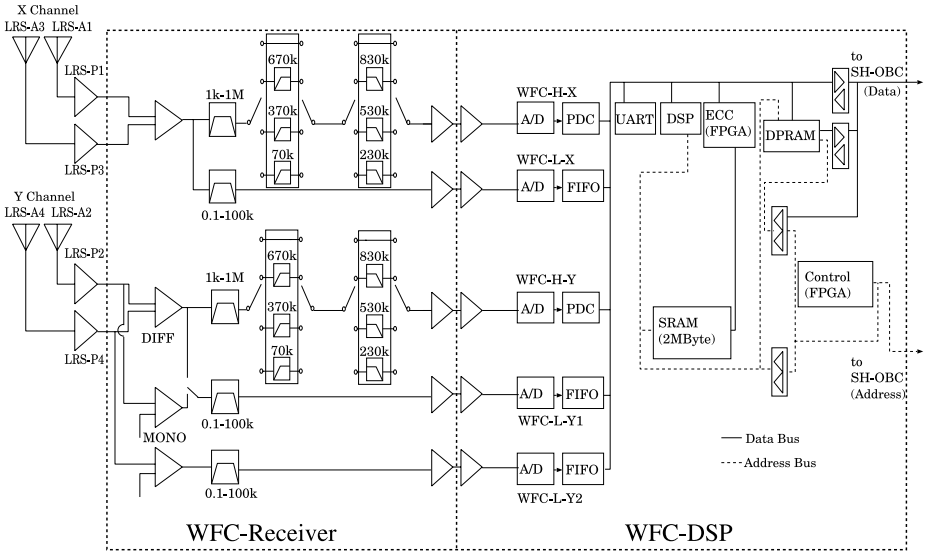

Fig. 13 A block diagram of the WFC receiver

two boards: WFC-Receiver and WFC-DSP. The former is used for the analog circuits, and the latter for digital circuits.

The WFC is a software receiver (Hashimoto et al. 2003) in which most of the functions are realized by a digital signal processor (DSP) and programmable down converters (PDC). Since the discovery of electrostatic solitary waves (ESW) by the GEOTAIL spacecraft,

the importance of waveform measurements has been highly recognized (Matsumoto et al. 1994a, 1994b). It is also important to measure wave fields with high-time and -frequency resolution for the investigation of plasma dynamics in a micro-scale. However, the amount of raw data from the plasma wave instrument is too huge to downlink all data to the ground because the scientific objectives require a wide coverage of frequency range. Digital signal processing onboard the spacecraft is useful because many kinds of operational modes can be implemented in the onboard software on a DSP without changing the hardware configuration.

3.3.4.1 WFC-H The WFC-H is a fast-sweep frequency analyzer covering the frequency range from 1 kHz to 1 MHz. The WFC-H has two channels of signal input module (WFC-H-X and WFC-H-Y). Differential signals from two pairs of orthogonal antennas are fed into WFC-H-X, and WFC-H-Y, respectively. The signals are first passed through by the high-pass filter (HPF) and low-pass filter (LPF) with cut-off frequencies of 1 kHz and 1 MHz, respectively. Two taps of 20 dB-gain amplifier are equipped and we can select the gain of input signals at 0 dB (low gain), 20 dB (middle gain) and 40 dB (high gain). In order to prevent saturation of the gain amplifiers caused by the intense input signals at an undesired frequency range, three optional HPFs and three optional LPFs are also implemented followed by the gain amplifiers.

The output signals are then digitized by two A/D converters. The A/D converter is a 16-bit and high-speed oversampled chip named AD9260 (Analog Devices 2000). The signals fed to the A/D converters are oversampled at a frequency of 20 MHz and signals at $f_s = 2.5$ MHz (8× oversampling) are fed to the PDCs. The HSP50214BVI (Intersil Corporation 2000) has been adopted as a PDC. The signals are down-converted by digital mixers and a quadrature numerical controlled oscillator (NCO) and filtered by three taps of decimation filters in the PDCs. The WFC-H sweeps a whole frequency range up to 1 MHz by changing the local frequency f_c of NCO controlled by the onboard software. In the nominal operation, two kinds of sweep pattern, a frequency range below 9.77 kHz with a frequency resolution of 38.2 Hz and a whole frequency range up to 1 MHz with a frequency step of 39.06 kHz, are alternately driven within 1 second. In order to reduce the amount of telemetry data, fewer numbers of data are taken out from the PDC output in the higher frequency band and thus the frequency resolution becomes coarser at a higher frequency range. The basic principle of the fast-sweep frequency receiver using PDC is described in the paper by Hashimoto et al. (2003). Because KAGUYA is three-axes stabilized, it is important to measure the phase difference of the signals measured by the two pairs of antennas to determine the polarization of the wave. Therefore, the A/D converters and PDCs for the WFC-H are controlled by the onboard software to obtain the exact timing of the wave signals. The detailed parameters applied to the LRS/WFC-H are seen in the paper by Kasahara et al. (2008).

There are three operation modes for the WFC-H: WAVE, FFT, and PHASE. In the WAVE mode, the down-converted and decimated data of in-phase and quadrature components of the signal, which are the raw output data, are directly packed into the mission data. In the FFT mode, the spectrum data are processed with the Fast Fourier Transform (FFT) by the onboard software, and the intensity at each frequency point is transported to the ground. In the PHASE mode, the output data from the two PDCs are processed with the FFT, and the intensity and phase difference between X and Y components at each frequency point is transported to the ground.

3.3.4.2 WFC-L The WFC-L measures waveforms below 100 kHz. As shown in Fig. 13, there are three channels of signal input module: WFC-L-X, WFC-L-Y1 and WFC-L-Y2. The WFC-L-X gives a differential signal between LRS-A1 and LRS-A3. The WFC-L-Y1 has two operation modes: differential and interferometry. In differential mode, the differential signal between LRS-A2 and LRS-A4 is fed to the WFC-L-Y1. In the interferometry mode, the signal from LRS-A2 is fed to WFC-L-Y1, and that from LRS-A4 is fed to WFC-L-Y2. This mode is dedicated to measuring the phase velocities and wave numbers of the observed plasma waves.

In the analog circuits of the WFC-L, the signals are first passed through by the HPF and LPF with cut-off frequencies of 100 Hz and 100 kHz, respectively. Since the 100 Hz HPF is a first-order RC filter and the intensities of low-frequency emissions increase inversely proportional to frequencies, the observable lowest frequency is virtually much lower. Two taps of 20 dB gain amplifier are equipped and we can select the gain of input signals at 0 dB (low gain), 20 dB (middle gain) and 40 dB (high gain). The gains of the WFC-H and the WFC-L can be independently controlled by command.

These three signals are then digitized by three A/D converters and fed into three First-In, First-Out (FIFO) chips separately. Taking advantage of the characteristics of switched-capacitor A/D converters, the waveform in the frequency range below 100 kHz with a sampling frequency $f_s = 250$ kHz or 50 kHz with $f_s = 125$ kHz is easily switched over by changing the clock frequency of the A/D converter by command. The A/D converter applied for the WFC-L is also AD9260 (Analog Devices 2000), so that the original sampling rate is 2 MHz and 1 MHz for $f_s = 250$ kHz and 125 kHz ($8\times$ oversampling), respectively.

Because the data rate of the raw waveform data produced by the A/D converters is far greater than the data rate capacity of the telemetry, the waveform data are intermittently acquired as follows. In the first step, the onboard software in the DSP begins to store the continuous waveform data into the memory until the storage area becomes full. These stored data are then processed by the DSP and transported to the ground over dozens of seconds. We also implemented the following functions in the onboard software to maximize our scientific output under the restriction of the telemetry budget.

Digital Filtering A digital decimation filter is implemented as an optional function in the DSP. The filter is an LPF with its cutoff frequency of $1/4\ f_s$ and a decimation rate of 2. This decimation filter can be cascaded with 3 taps at most; therefore the maximum frequency and amount of downlink data can be reduced down to $1/2$, $1/4$ and $1/8$. Then the corresponding duty ratio (the ratio of the observation duration to the data transportation duration) can be raised by 2, 4, and 8 times, respectively. Selecting the number of taps to be used for data processing in the DSP by command, we can change the maximum frequency of the WFC-L.

Automatic Filter Selection "Automatic filter selection" mode was implemented on the onboard software. In this mode, the onboard software evaluates maximum amplitudes or averaged powers at each frequency band to determine whether to select an intermittent measurement covering higher frequency range with a lower duty ratio or a semi-continuous measurement in the lower frequency range. Because the waveform observation is generally more important in the lower frequency range from a scientific point of view, signals in the higher frequency range weaker than the threshold level are automatically eliminated by the above mentioned optional decimation filters in the DSP and the decimated waveform data is packed into mission packets. This technique makes it possible to downlink the significant waveform to the ground in shorter time duration and to capture a new series of waveform data with a higher duty ratio. The threshold level for the decision at each frequency range

can be changed by command, and adequate threshold levels were set up by analyzing a certain amount of data after launch.

Data Compression We adopted a range coder that is one of lossless compression algorithms (Range Coder Homepage 1999). According to our estimation in the software design, the compression ratio is ∼75% at most, but we gave priority to the precision of waveforms over the compression ratio because lossy compression for a wide frequency range (<100 kHz) might have a bad influence on the nature of waveform in case several kinds of wave phenomena are simultaneously observed. In addition, the computational load of lossy compression was too heavy and sacrifice of the other software functions was inevitable if we adoptet the lossy compression method.

3.3.4.3 Cooperative Measurements with SDR Subsystem The SDR is an active system using an HF radar technique to investigate the surface and subsurface structure of the moon. When the SDR is in operation, a sounder pulse is transmitted every 50 msec. The WFC is, therefore, designed to perform during the time gaps of sounder pulse transmission in order to avoid interference from the pulses. Especially for waveform measurements of the WFC-L, the waveform becomes discontinuous every 50 msec when the SDR is in operation because of the interruption. The interruption points are recorded in the mission packet according to the status bits of the WFC-L's FIFOs. The default interval of suspension is set at 4.9 msec.

3.3.5 Antenna Deployment Controller

The antenna deployment controller operates the driving motor of the antenna deployment mechanisms, which has monitoring limit switches for detection of full extension and retraction of antenna elements, and a potentiometer for measurement of deployment length. Power for driving the motors (28 V × 100 mA for each) is also supplied by the antenna deployment controller. Due to limitations of the LRS-E power supply, simultaneous deployment of two or four antenna is not possible. Four antenna elements were, therefore, deployed one by one.

3.3.6 Power Supply

The power supply is a DC-DC converter which converts the primary power source with a voltage range from 32 V to 52 V provided by the spacecraft to the secondary power sources with voltages of +5 V, +12 V, −12 V, and +28 V for providing each subsystem of LRS. The power sources with voltages of +2.5 V and +3.3 V for field programmable gate arrays (FPGAs) in the SDR receiver and WFC receiver are generated from the secondary power source with a voltage of +12 V. The power source with a voltage of 45 V for sounder pulse transmission is generated from the secondary power source with a voltage of +28 V.

3.3.7 Data Processing Unit

For the purpose of onboard data processing, control and status monitor of the instruments, one mother data processing unit called the SH7708 OnBoard Computer (SH-OBC) and two daughter Digital Signal Processors (DSP) are utilized in LRS system.

SH-OBC is circuit board with three SH7708 processors (Renesas Technology), which is also used in other instruments onboard the KAGUYA spacecraft. Because the SH7708 processor does not have enough tolerance to cosmic radiation, SH-OBC works by majority decision rule among three processors. Operating frequencies of the processor and I/O bus

are 60 MHz, and 15 MHz, respectively. SH-OBC receives commands from the DHU of the spacecraft for control of the instrument. The SH-OBC sends house keeping (HK) status to the DHU every one second. In standard- and low-bit rate operation (176 kbps and 4 kbps), the SH-OBC produces the data packets and sends them to the transfer frame generator (TFG) of the spacecraft, which acquires data packets and sends them to the telemetry or onboard data recorder.

In order to process the waveform data obtained by the SDR receiver and WFC receiver, two DSP devices, SMJ320C31GFAM50 (Texas Instruments), are used in the LRS system. The operating frequency of the DSP is 50 MHz. In high-bit rate operation (492 kbps), DSP produces data packets and directly sends them to TFG of the spacecraft.

3.3.8 Onboard Software

A flow chart of onboard software for SH-OBC is shown in Fig. 14. After initializations of the interrupt tables and variables, the main loop is initiated with a period of 50 msec. In this loop, the system is receiving commands and predicted orbit data from spacecraft DHU, acquiring of data packets from dual-port memory which is shared with DSP, and sending HK status to spacecraft DHU. The received commands and data packets are stored in the buffer. Command execution and data packet transfer to the TFG of the spacecraft are carried out in the main loop.

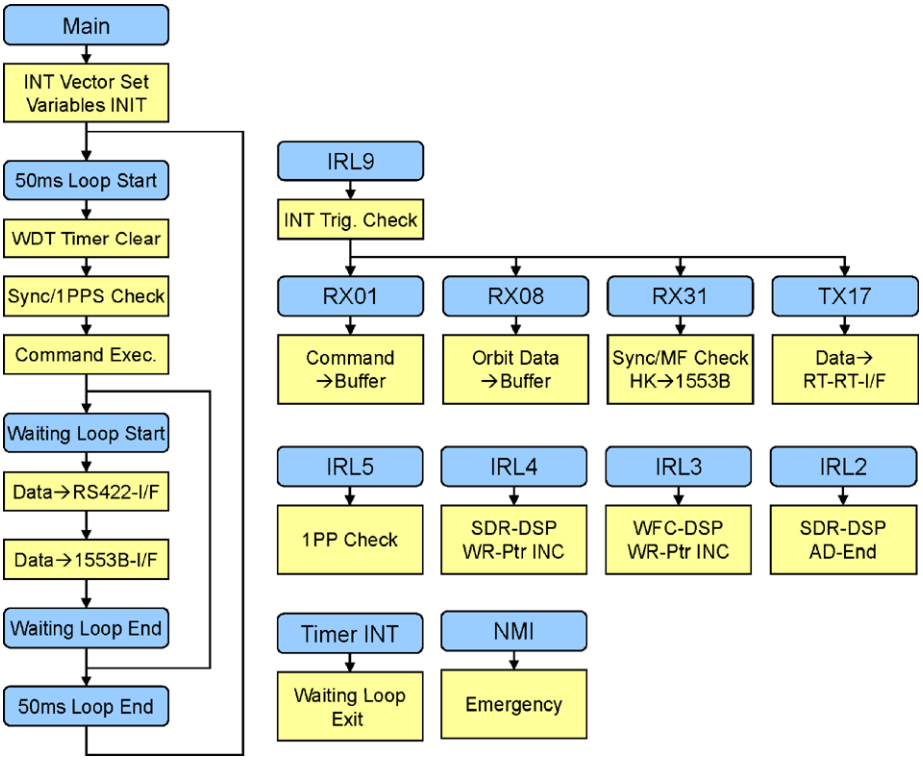

Fig. 14 Flow chart of onboard software for SH-OBC. After the initialization of interrupt table and variables, the main loop starts with a period of 50 msec. Commands, HK statuses, and data packets are processed in interrupt routines

The onboard software is designed to perform operations in many observation modes. However, except for a few nominal observation modes, most of them were never used in the flight operations. In some emergency cases, some of them are useful for continuation of observations. The packet ratio between the WFC-L and WFC-H can be changed by command. In the nominal operation, the packet ratio between the WFC-L and WFC-H was 8:2 in the WFC/80 kbps and WFC/160 kbps operations, while only the WFC-H was operated in the other operation modes except in the period of the last part of the extended mission (see Sect. 4.5). We also implemented WFC-DUMP function as a special mode, in which the mission packets of WFC-L are once stored in the memory of SH-OBC and are restored by a DUMP command later, but it was not used in the flight operations.

4 Operation

LRS had been operated from the antenna deployment on October 29, 2007 until the spacecraft impacted to the moon on June 10, 2009. The operation time of each observation mode is summarized in Table 4. We have successfully obtained 2363 hours worth of radar sounder data and 8961 hours worth of natural radio and plasma wave data. Figure 15 shows the coverage of the radar sounder data shown by a topographic map based on the surface echo data obtained by LRS. Figure 15(a) shows coverage of both the SDR-W and SDR-A modes. Figure 15(b) shows that of the SDR-W mode only. The radar sounder observation covers almost all areas on the moon. There are, however, some gaps of observation in the coverage of SDR-W mode only. In order to perform advanced analysis such as SAR analysis, SDR-W data with a time resolution of 50 msec is more useful than SDR-A data with a time resolution of 400 msec. We were planning to fill those observation gaps in the nominal operation period until October 31, 2008. However, due to the hardware trouble which occurred on September 10, 2008 (as described below), we had to give up the supplement observations.

The operation period of LRS can be divided into five stages: (1) Electromagnetic compatibility (EMC) checkout operation, (2) Nominal operation with standard downlink rate, (3) Nominal operation with enhanced downlink rate, (4) Observation halt due to hardware trouble, and (5) WFC-4kbps operation in low-altitude orbit.

Table 4 Operation time of each subsystem mode in a period from October 29, 2007 to June 10, 2009

Subsystem	Operation Mode	Each [hours]	Total [hours]
SDR	SDR-W/488 kbps	1726	2363
	SDR-A/80 kbps	637	
NPW	NPW-W/488 kbps	334	6570
	NPW-DS/16 kbps	2234	
	NPW-PL/16 kbps	414	
	NPW-DS/2 kbps	740	
	NPW-PL/2 kbps	485	
	NPW-A/16 kbps	637	
	NPW-S/4 kbps	1726	
WFC	WFC/160 kbps	2648	8961
	WFC/80 kbps	637	
	WFC/4 kbps	4451	
	WFC/2 kbps	1225	

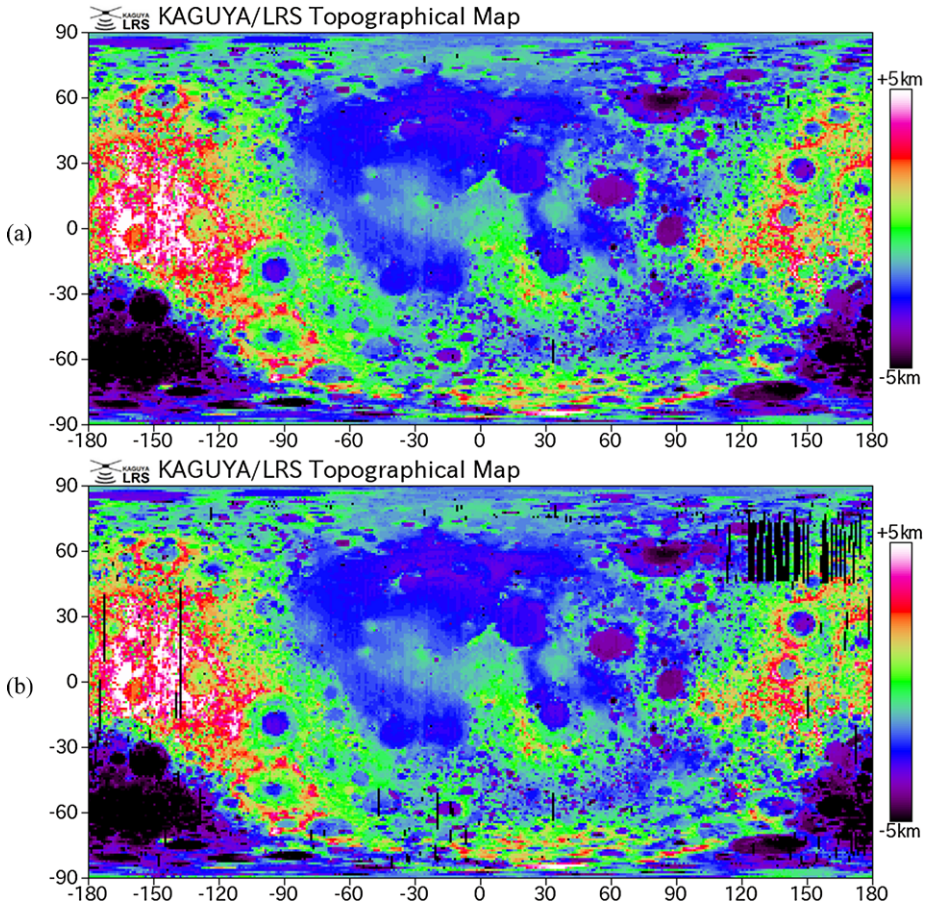

Fig. 15 Coverage of radar sounder data shown by a topographic map based on the surface echo data obtained by LRS. Panel (**a**) shows coverage of both SDR-W and SDR-A data. Panel (**b**) shows coverage of SDR-W data only

4.1 EMC Checkout Operation (October 29, 2007–December 15, 2007)

After the transfer of the KAGUYA spacecraft into final lunar orbit, an antenna deployment operation was performed on October 29, 2007. Due to limitations of the power supply of LRS-E, the antenna elements of LRS-A1, A2, A3 and A4 were deployed sequentially. The antenna deployment operation was successfully completed. After the antenna deployment operation, the initial function checkout of the LRS passive observation was carried out. It was confirmed that there were not any anomalies on function and performance of the passive observation. Just after the initial function checkout, continuous natural radio and plasma wave observations were carried out for the purpose of EMC checkout. During this period, SDR subsystem was suspended, and NPW and WFC subsystems were operated in NPW-W/488 kbps, NPW-DS/16 kbps, WFC/160 kbps, and WFC/4 kbps.

In order to detect weak sounder echoes and planetary radio waves, strict EMC controls were applied to the total system of the KAGUYA spacecraft (Kumamoto et al. 2008). As a result of strict EMC controls on the ground, most instruments were quiet enough to allow

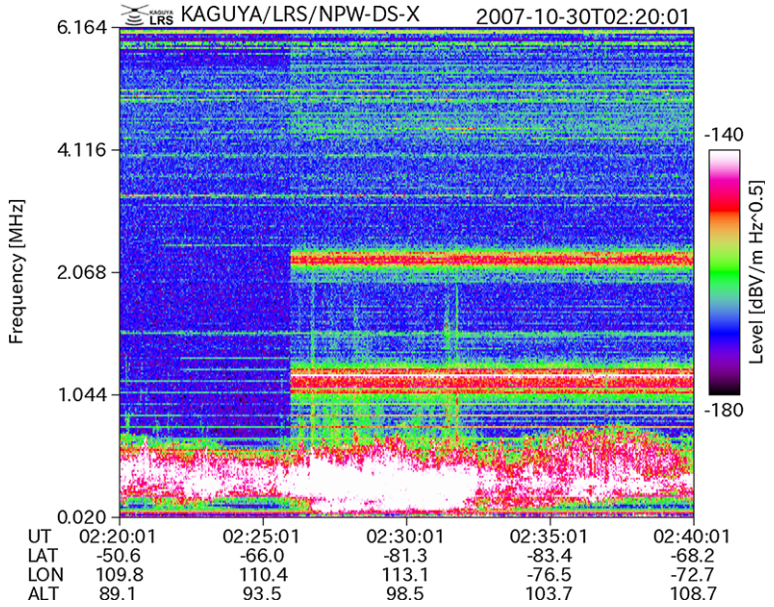

Fig. 16 The spacecraft power supply noises at about 1 MH and 2 MHz. Frequency steps are linearly allocated between the labels. The noises occur when the spacecraft moves into the dayside. The background noise level also increases with several dB in wide frequency range. The emissions below 700 kHz are AKR

detection of sounder echoes as intense as background galactic noise, or −190 dBW/m^{2}Hz (Dulk et al. 2001). However it was found that there were severe noises caused by the power supply system of the spacecraft while the spacecraft was in the dayside. Figure 16 shows an example of natural radio and plasma wave data obtained on October 30, 2007. KAGUYA moved into the dayside at 02:26 UT (universal time). Intense noises appeared around 1 MHz and 2 MHz. Not only at 1 MHz and 2 MHz but also in wide frequency range, noise levels slightly increased with a few dB. The noises are previously found in the EMC test on the ground. We however interpreted these as noises caused by test equipment simulating the solar array panel. The interpretation was incorrect. The noise was not caused by the solar array panel simulator but by the spacecraft power supply system in conditions in which the currents were supplied from the solar array panel in the dayside (or from the solar cell panel simulator in the ground test). It should be noted that the solar array power conversion system can be a severe noise source. It has to be checked more carefully in the EMC tests in the future spacecraft developments.

Noise levels of the WFC receiver were also evaluated during this period. The spectra measured by the WFC-H were shown in Fig. 17. The red line is a spectrum measured in the final system function test of KAGUYA performed at the Spacecraft Integration and Test Building (SITE) in the Tsukuba Space Center (TKSC) of JAXA on February 12, 2007. At that time the LRS antennas were all retracted in the spacecraft body and this spectrum shows the internal noise level of the WFC receiver. The black broken line shows the specification of the EMC RE (Radiated Emission) level required for the instruments outside the spacecraft panels of the KAGUYA main orbiter. The green line is a spectrum measured at 18:30 UT on November 2, 2007. The moon was located in the solar wind and KAGUYA was located in the shade of the sun at this moment. That is, KAGUYA was in a plasma cavity called the lunar wake. We verified that there were no significant wave activities so that this line

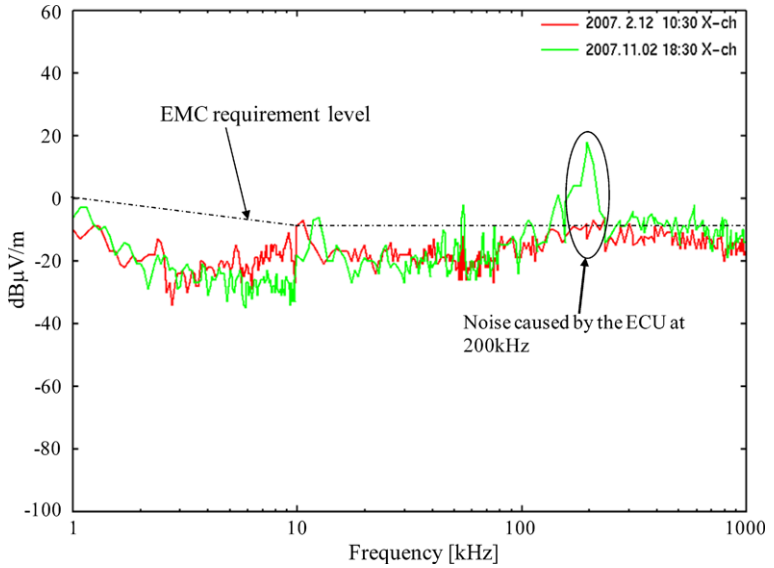

Fig. 17 Evaluation of noise level of the WFC-H performed in the initial check-out phase. *Red line* is a spectrum measured in the final system function test in the Tsukuba Space Center of JAXA and *green line* is a spectrum measured at 18:30 UT on November 2, 2007. *Black broken line* shows the specification of the EMC (Electro-Magnetic Compatibility) RE (Radiated Emission) level required to the instruments outside the spacecraft panels of the KAGUYA main orbiter

indicates the noise level of the WFC after launch. The noise levels before and after launch (red and green lines) were almost the same and well below the specifications of the EMC RE level except for the narrowband noise at 200 kHz. The narrowband noise at 200 kHz, which exceeded the specifications of the EMC RE level by ∼30 dB, was caused by the ECU (Electronic Control Unit) for the Solar array drive mechanism controlling the attitude of the solar array paddle. It is also noted that it is important to take more care of a noise originated from the solar array drive mechanism in the EMC tests in the future spacecraft developments.

4.2 Nominal Operation with Standard Downlink Rate (December 15, 2007–June 6, 2008)

Nominal operation started on December 15, 2007. In advance of nominal operation start, the initial function checkout of the sounder observation was performed on November 20 and 21, 2007. The initial checkout of the sounder transmitter was delayed from the checkout of the passive system to avoid turning on the high voltage instruments in the out gas from the instruments onboard the spacecraft. It was confirmed that there were not any anomalies on function and performance of the sounder transmitter and receiver. The saturation level of the SDR receiver with high gain was, however, almost equal to that of surface echoes, and sometimes lower. We therefore selected medium gain in the nominal operation.

Due to limitations of the downlink rate of the spacecraft, the upper limit of the LRS data rate was 14.2 Gbits/day. The data rate was far lower than that for 24-hour SDR-W/488 kbps operation. Of course SDR-W/488 kbps operation was performed as much as possible based on availability. We also have to select SDR-A/80 kbps, NPW-DS(PL)/16 kbps, WFC/160 kbps, and WFC/80 kbps operations (176 kbps) and even NPW-DS(PL)/2 kbps and WFC/2 kbps operations.

Since the SDR is needed to use one of two pairs of antennas as transmission antennas (nominally LRS-A1 and A3), the WFC used another pair (LRS-A2 and A4) of the receiving antennas under the operation of the SDR. On the other hand, two pairs of antennas were used when the SDR was not in operation.

4.3 Nominal Operation with Enhanced Downlink Rate (June 6, 2008–September 10, 2008)

In the early phase of the nominal operation, the upper limit of the LRS data rate was 14.2 Gbits/day because we were not experienced in the operation of KAGUYA and we could not allocate enough time for data downlink. However, after gaining operational experiences, we were able to allocate more time for data downlink. Based on the possible downlink rate in the actual operations, the upper limit of LRS data rate was revised to 21.3 Gbits/day since June 6, 2008. The upper limit of the LRS data rate was further increased to 42.6 Gbits/day in the period when KAGUYA's orbit is in a longitude around 90° and KAGUYA is always visible from the Earth. Thanks to the increased data rate, we were then able to select SDR-W/488 kbps operation more frequently. The NPW-DS(PL)/16 kbps and WFC/160 kbps operations and even NPW-W/488 kbps operation could also be selected in this period. The coverage of sounder data was drastically increased. Several events of Jovian hectometric (HOM) radiation were also detected in this period.

As for WFC, the following operations were performed in this period.

The interferometry operation of the WFC-L was performed from June 20, 2008 to September 8, 2008 once or twice daily. The observation duration of the interferometry mode was ∼20 minutes per one operation. The maximum frequency of the WFC-L waveform was set at 25 kHz so as to measure phase difference and polarity of electrostatic solitary wave (ESW) on the condition that plasma frequency could be simultaneously observed as the plasma frequency is expected to be lower than 25 kHz. We also expect the detection of the dust impact to the spacecraft body in this operation mode.

The automatic filter selection mode of the WFC-L was performed from June 20, 2008 to August 13, 2008 once or twice daily. The observation duration of this mode was ∼20 minutes per one operation. We evaluated the WFC-L data accumulated by the end of May, 2008 and determined the appropriate threshold level taking into account the average power of the natural wave at each frequency band.

4.4 Observation Halt Due to Hardware Trouble (September 10, 2008–February 19, 2009)

On September 10, 2008, LRS unexpectedly failed to turn on. Nominal operation was stopped and failure investigations were started. As a result of these investigations, we concluded that the failure was associated with start up of one FPGA device, XQVR300-4CB228M (Xilinx). A dependence on temperature was also discussed. On November 8, 2008, the FPGA normally started up after the 6-hour heat run and passive measurements by the NPW and WFC were tentatively recovered for ∼30 hours. However it could not start up again on other days even after the long heat run. It is inferred that cosmic radiation created an aging effect on the FPGA. The FPGA includes the controller of the SDR-DSP, AD converter for SDR and NPW receivers. Continuation of sounder observations and natural radio and plasma waves in HF range thereafter was difficult. In addition, the FPGA also includes the controllers of the power supply switch for the LRS-P units. Although the WFC receiver did not have any trouble, it was impossible to continue observations because the malfunctioning FPGA could not turn the LRS-P on.

4.5 Extended Operation with WFC-4 kbps in Low Altitude Orbit (February 19, 2009–June 10, 2009)

We therefore decided to give up continuation of sounder observations and natural radio and plasma wave observation with SDR and NPW receivers, and to try to turn on the LRS-P again and restart the observation by WFC receiver. Because the power supply switch for the LRS-P units is a latching relay, we can keep LRS-P units on without using the troubled FPGA if we can turn it on just once more. After the numerous trials for turning on the FPGA, we could successfully turn on the FPGA on February 19, 2009. We simply turned on LRS-P units by using the FPGA, and turned off the FPGA in order to avoid unexpected FPGA reset which turned the LRS-P units off again. We finally restarted natural radio and plasma wave observations by the WFC receiver. Because the FPGA had trouble being turned off, the SDR and NPW receivers could not be operated again in this period. KAGUYA spacecraft had already descended to 50 km altitude since February 1, 2009 in order to perform observations of magnetic fields and energetic particles in the vicinity of the magnetic anomaly on the lunar crust. The plasma wave data obtained in this period will make important contributions on studies on plasma processes around the magnetic anomaly.

The WFC observations were continuously performed, except for several suspensions due to a radiation problem, until KAGUYA impacted on the south-east nearside of the moon on June 10, 2009. As the telemetry rate was limited at 4 kbps, we first performed spectrum measurements of the WFC-H with PHASE mode from February 19, 2008 to May 26, 2009. During this period, KAGUYA was lowered again to 10–30 km altitude (perilune) from April 16, 2009. Finally we made a waveform observation using the WFC-L during the last part of the extended mission from May 26, 2009 to the moment of the KAGUYA's impact to the moon on June 10, 2009. The data rate of 2 kbps was assigned to one component (WFC-H-X) spectrum in FFT mode, and the rest of 2 kbps was assigned to waveform data from WFC-L-X below 12.5 kHz.

5 Initial Results of Radar Sounder Observations

Radar sounder observations had been successfully performed since the start of nominal operation on December 15, 2007 until the occurrence of hardware trouble on September 10, 2008.

The analysis flow of radar sounder data is as follows: Transmission and receiving of the sounder pulse are performed with intervals of 50 msec. The RF echo signal detected by LRS-A is fed to the SDR receiver and mixed with local signals. The frequency of the RF signal and local signal sweeps from 4 MHz to 6 MHz with a rate of 2 MHz/200 μsec. The delay time from the RF signal to the local signal is changed depending on the spacecraft altitude. After mixing with a local signal, the IF waveform is captured with a sampling frequency of 6.25 MHz. Sampling data number at one-time capture is 2048. The IF waveform data are sent to the ground via the telemetry. Performing Fourier transform of each IF waveform data in the analyses on the ground, we can obtain an A-scan plot, or echo power to range plot. By making a series of A-scan plots obtained in different locations as the spacecraft moves along the orbit, we can obtain a B-scan plot, or depth-to-location plot, which is also called a radargram. The KAGUYA/LRS data are returned to the ground without any onboard compression. It enables us to perform flexible data analyses on the ground for improvement of radargram quality.

Raw radargrams often contain not only echoes from large-scale horizontal reflectors, such as moon surface and subsurface boundaries between geophysically different media,

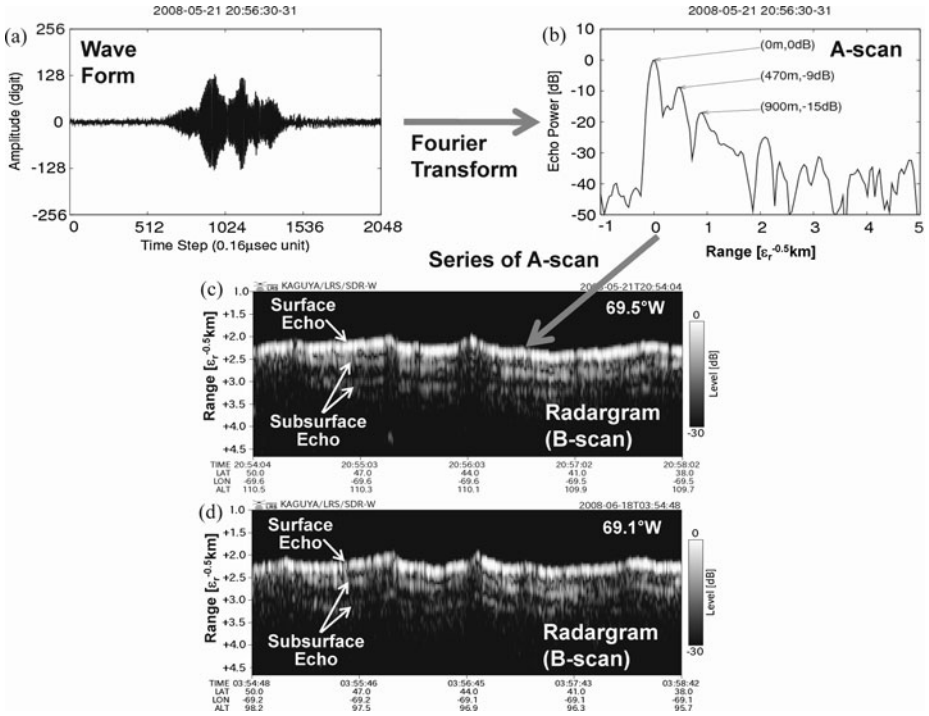

Fig. 18 (**a**) The waveform of sounder echo, (**b**) Ascan plot derived from the waveform data, (**c**) radargram in longitude of 69.5°W made by series of A-scan plots, and (**d**) radargram in longitude of 69.1°W

but also echoes from off-nadir point reflectors, such as crater edges, and background noises. In order to identify the echoes from horizontal subsurface reflectors in the radargrams, we have produced running averaged radargrams in the analyses on the ground. Running average will be an effective method for intensification of echoes from horizontal reflectors and suppression of other echoes and background noises. Figure 18 shows the analysis flow for the generation of the running averaged radargram. First, we obtained averaged IF waveforms made from 20 raw IF waveforms (Fig. 18(a)). Then, by performing a Fourier transform of running averaged IF waveforms, we can obtain an A-scan plot (Fig. 18(b)). By making a series of A-scan plots, we can obtain a running averaged radargram (Fig. 18(c)). Figure 19 shows the comparison between radargrams generated by raw IF waveforms and by running averaged IF waveforms. As shown in Fig. 19(a), it is difficult to identify subsurfcae echoes in the raw radargram due to high noise levels. There are also surface echoes from off-nadir directions. Crater edges and other surface structures often become effective reflectors of the radio waves. The range from the spacecraft to the reflector decreases while the spacecraft moves toward the reflector, and increases while the spacecraft moves away from the reflector. The off-nadir echo therefore shows hyperbolic structure in the radargram. On the other hand, the range from the spacecraft to the subsurface reflector is expected to be almost constant if the structures of subsurface reflectors are horizontal. The running average is therefore effective not only for background noise reduction but also for reduction of off-nadir echoes and intensification of the echoes from horizontal subsurface structures as shown in Fig. 19(b). If the surface reflectors distribute along the line parallel to the footprint

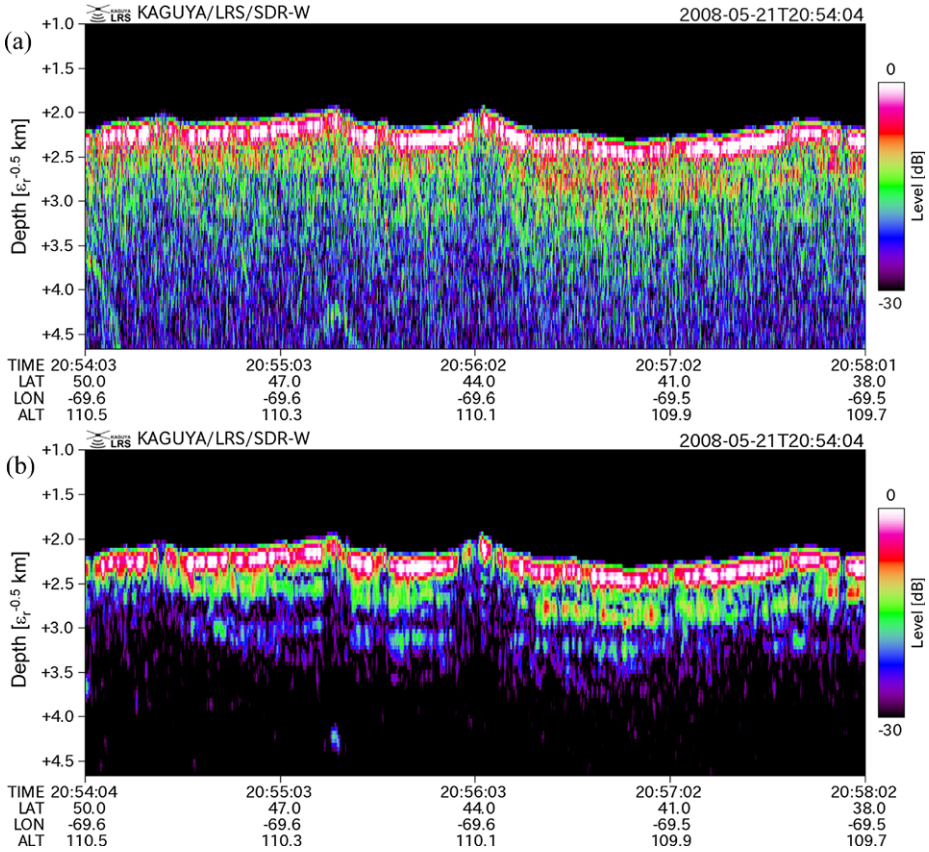

Fig. 19 (**a**) The radargram derived from the raw data and (**b**) the radargram derived from the running averaged data in the nearside maria

of the spacecraft, the range from the spacecraft to the surface reflectors could be constant. The hypothesis can be denied by comparison with the radargrams in a different longitude as shown in Fig. 18(d). If the reflector is on the surface in off-nadir directions, the reflector range should be different in radargrams along different longitudes. However, as shown by Figs. 18(c) and 18(d), there is no difference between the reflector ranges in radargrams observed in different longitudes. It can be therefore concluded that the echoes are not from surface reflectors but from sub-surface reflectors.

If the range from the KAGUYA to the reflectors changes over $\lambda/2$, or 30 m, during transmission of 20 pulses, or 1 sec, the running average suppresses not only noise levels but also the echo levels from the reflectors due to phase mixing among the averaged echo signals. The altitude of KAGUYA was maintained within 100 ± 30 km. The orbital period of KAGUYA was about 2 hours. The average vertical velocity of KAGUYA is therefore estimated as <17 m/sec. It is therefore concluded that the echo level from the subsurface reflectors with horizontal structures is not suppressed by the running average. On the other hand, the echo level from the off-nadir surface reflector was effectively suppressed because the range from the KAGUYA to the off-nadir surface reflector changes with horizontal velocity of KAGUYA, 1.6 km/sec. The running average is thus useful for identification of

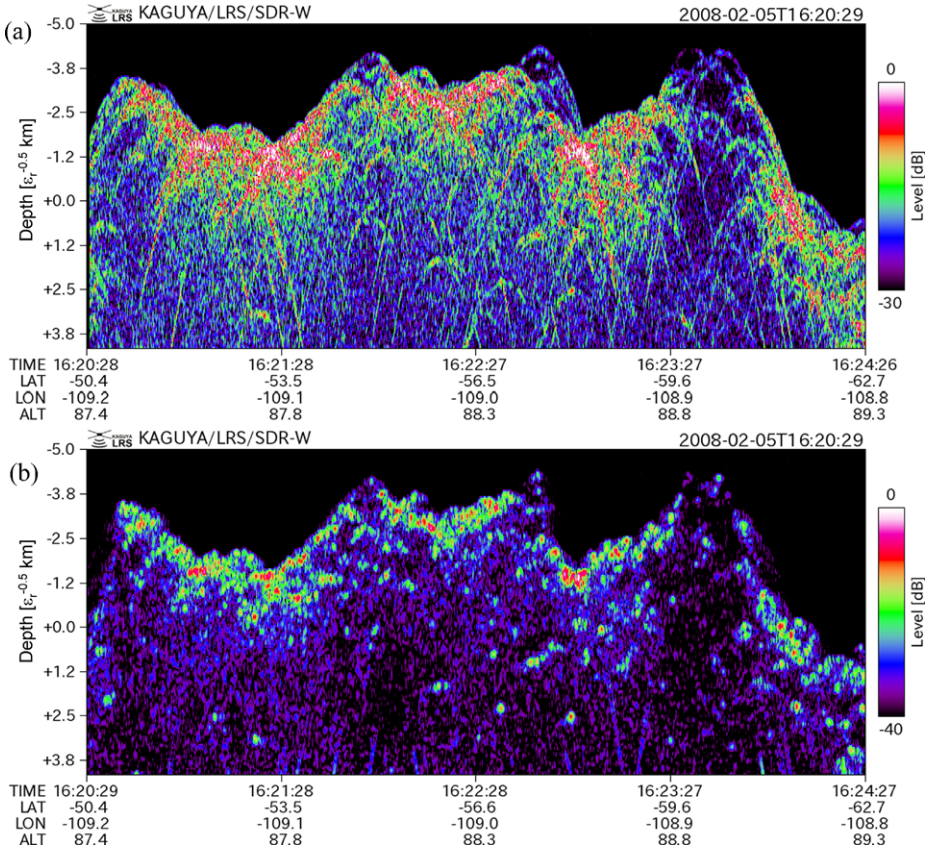

Fig. 20 (**a**) The radargram produced from the raw data and (**b**) the radargram produced from the running averaged data in the high land regions

the subsurface reflectors in general. However, it should be noted that the running averaging method is useless for the following subsurface structures: (1) subsurface reflectors with slope, and (2) subsurface point reflectors. Echo signals from sloped reflectors with a gradient of >1 degree ($\tan^{-1} 30$ m/1.6 km) will be suppressed due to phase mixing. The subsurface point reflectors are also suppressed as are the surface point reflectors. We do not intend to find every kind of subsurface structure with this simple method.

Figure 20(a) shows a typical example of a radargram obtained in the farside highland regions. The identifications of the subsurface echoes in the farside highland regions and polar regions are difficult in general because the structures of the off-nadir surface echo curves are more complex than in the nearside maria due to the roughness of the surface structure. The running average is also useless in the farside highland regions as shown in Fig. 20(b). In order to solve the problems and achieve the analyses of global subsurface radar sounding data, it would be useful to apply SAR analyses (Kobayashi et al. 2002a, 2002b; Kobayashi and Ono 2006, 2007) and to perform simulations of off-nadir surface echoes to be removed based on a digital elevation model of the lunar surface which will be provided by Laser Altimeter (LALT) (Araki et al. 2008, 2009) and Terrain Camera (TC) (Haruyama et al. 2008) onboard the KAGUYA spacecraft.

In order to suppress the hyperbolic-pattern echoes caused by the off-nadir point reflectors, the multiple Doppler filters were implemented in MARSIS onboard the Mars Express (MEX) (Picardi et al. 2004; Jordan et al. 2009). The frequency differences between the echo signals and the reference chirp signal depend on the ranges between spacecraft and targets, and the velocity of the spacecraft. Echoes from the surface/subsurface point reflectors can be selected by the Doppler filters and compressed by onboard data processing in order to reduce the downlink data rate. The data processing is a kind of unfocused SAR, which can be applicable even for onboard data processing with limited computational resources. Doppler filters were not implemented in LRS onboard data processing. Instead, we intend to apply focused SAR processes (Kobayashi and Ono 2007) to the downlinked waveform data. The processing is currently being carried out and the results will be published elsewhere.

Several initial results of radar sounding of the lunar subsurface structures have been reported based on the observations in the nearside maria. Ono et al. (2009) reported that (1) distinctive echoes were discovered from apparent depths of several hundred meters in several nearside maria, and (2) that mare ridges in southern Serenitatis are the surface manifestations of anticlines made by mare basalts. It was also found that the folds do not have growth structures, indicating post-depositional deformations. Taking surface ages (Hiesinger et al. 2000, 2003) into account, it was suggested that the subsurface reflectors are buried regolith layers, and that the deformation is younger than 2.84 Ga. Oshigami et al. (2009) reported that clear subsurface echoes are found in 10% of the western nearside maria such as Mare Humorum, Mare Imbrium, and Oceanus Procellarum. They also pointed out that clear subsurface echoes were well found in the old-age area; the surface ages of most of the area are older than 3.4 billion years. As for the inhomogeneity of the clear subsurface echoes, Pommerol et al. (2010) made another suggestion that there was clear anticorrelation between the observation points of clear subsurface echoes and TiO_2-rich area. Olhoeft and Strangway (1975) reported that loss tangent of the surface media depends on the abundance of ilmenite. TiO_2-rich surface can cause the absorption of the subsurface echoes. The echo masking effect by TiO_2 should be taken into consideration when we investigate the radargrams obtained by lunar subsurface radar soundings. It can also be pointed out that the above results were achieved based on an almost fully-covered sounder observation first performed by KAGUYA/LRS.

6 Initial Results of Natural and Artificial Radio Wave Observations in 0.02–30 MHz

Natural radio and plasma wave observations in a frequency range from 0.02 to 30 MHz had been successfully performed since the start of the EMC checkout operation on October 29, 2007 until the occurrence of hardware trouble on September 10, 2008. Not only were natural radio waves such as AKR, Type-III solar radio bursts, and Jovian HOM observed, but also artificial radio waves such as broadcast radio waves from the Earth. Initial results are obtained as follows.

6.1 Auroral Kilometric Radiation (AKR)

Figure 21 shows a summary plot of the NPW receiver in a period from October 29, 2007 to September 10, 2008. The emission below 700 kHz is AKR. The apparent occurrence of AKR observed by LRS changes with a period of one month. It is however considered not to be because the occurrence of AKR itself changes with a period of one month, but because most AKR sources are located in the nightside of the Earth (Gurnett 1974; Green et al.

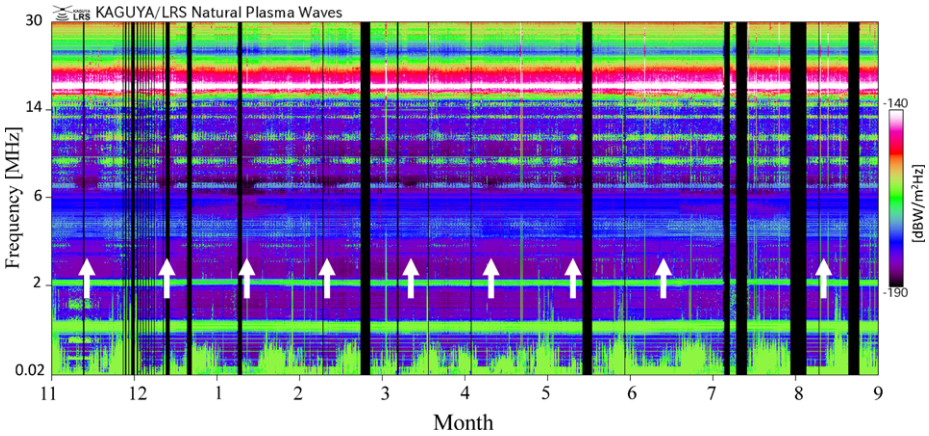

Fig. 21 Summary plot of NPW receiver in a period from October 29, 2007 to September 10, 2008

1977). AKR is more often observed when the moon and spacecraft were in the nightside of the Earth.

Figure 22(a) shows the spectrogram of AKR obtained by NPW-W mode observations with a time resolution of 100 msec and a frequency resolution of 6 kHz. We can see interference patterns on the spectrogram of the AKR. They are inferred to be caused by the interferences between the directly arrived AKR and the one reflected at the moon's ground surface (see Fig. 23). Figure 22(b) shows calculated interference patterns by assuming some AKR locations near the Earth. The frequency and time scale of the interference patterns are well reproduced.

Further analysis of the AKR interference pattern would be useful for studies on surface and subsurface echoes in a frequency range of several hundred kHz. Based on the maximum and minimum intensities of interfered AKR, we will be able to obtain reflectivity of the lunar surface, which is associated with electric permittivity and surface roughness.

Another interesting topic related to the AKR interference is verification of the existence of the lunar ionosphere. Because the frequency band of AKR covers f_p at the location of peak electron density reported by Vyshlov and Savich (1979), the AKR can be reflected by the lunar ionosphere if it exists. Goto et al. (2009) presented a new lunar ionosphere exploration method comparing an observed interference pattern with the theoretical ones derived from ray tracing. This is a new approach in examining the existence of the lunar ionosphere which is not based on the radio occultation technique.

6.2 Jovian Hectometric (HOM) Radiation

Nominal operations with an enhanced downlink rate from June 6, 2008 to September 10, 2008 increased the opportunities for selecting observation modes with SDR and NPW receivers with a high data rate. It enabled us to observe several events of Jovian hectometric (HOM) emissions. Figure 24 shows an example of Jovian HOM emission. Bursty emissions with large spectral structures are seen in the spectrogram. As for decametric (DAM) emissions, it was suggested that interplanetary scintillation causes those spectral structures (Genova and Boischot 1981; Genova and Leblanc 1981). The emission was also detected by WIND spacecraft (Bougeret et al. 1995) simultaneously. Jovian System III central meridian longitude (CML) of KAGUYA was 230°. Imai et al. (2008) derived CML dependence of occurrence probability of Non-Io DAM and HOM emissions in a frequency range from

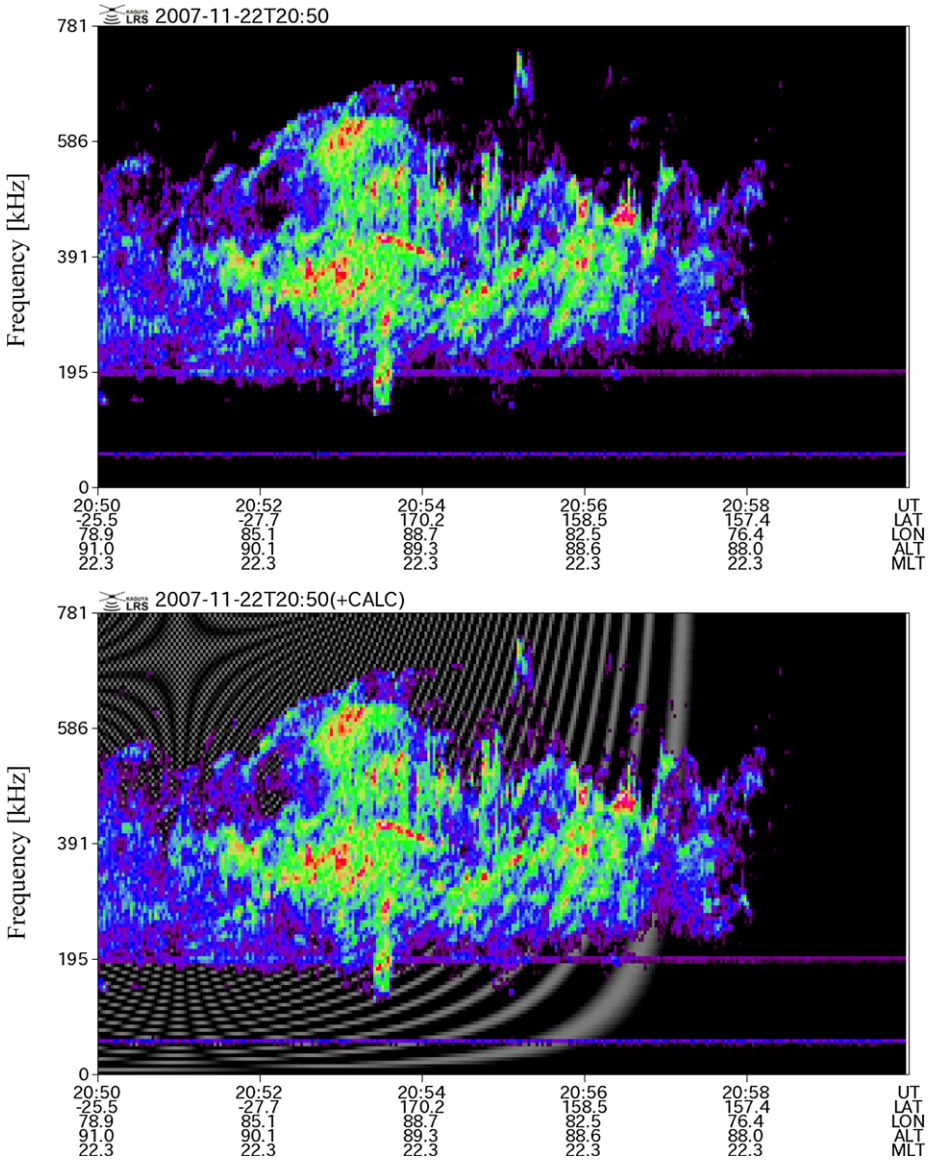

Fig. 22 Spectrogram of AKR with interference patterns. In Panel (**b**), the AKR spectrogram is superposed on the calculated phase difference between AKRs directly arrived and reflected at the moon surface

4 MHz to 16 MHz based on Cassini plasma wave data. They suggested that CML ranges of Non-Io-A and Non-Io-B DAM gradually became close and merged around 200° in a frequency range below 16 MHz. The event shown in Fig. 24 could be a low-frequency-extended Non-Io A/B DAM based on the CML of occurrence. On the other hand, Jovian DAM emissions have not been detected by LRS probably because the sensitivity is much worse above 15 MHz as shown in Fig. 21, where the noise level of LRS above 15 MHz is higher than -170 dBmW/m^2 Hz due to frequency dependence of antenna impedance and preamplifier input capacitance.

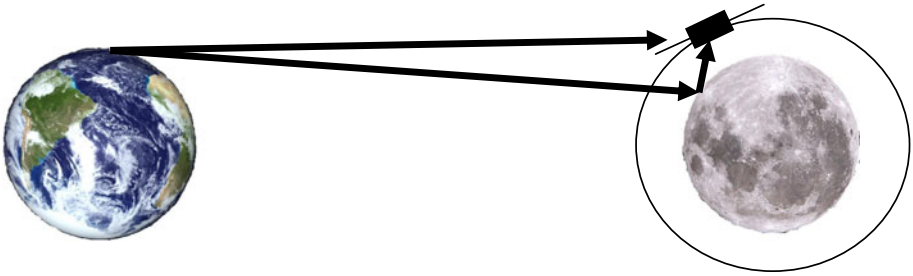

Fig. 23 Interference of AKRs between directly arrived and reflected on the lunar surface

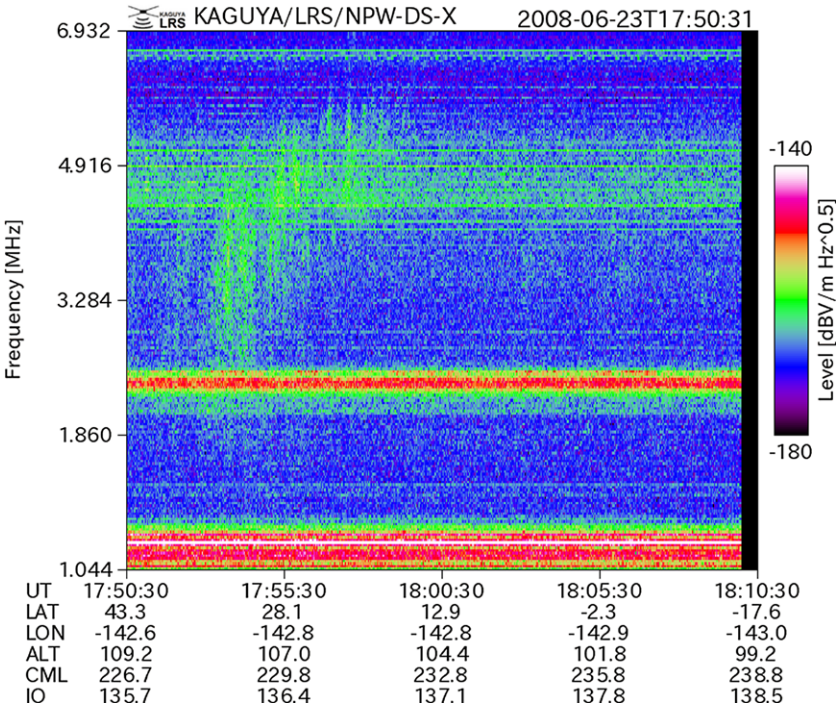

Fig. 24 An example of spectrogram of Jovian HOM. Frequency steps are linearly allocated between the labels

The observation of HOM by LRS demonstrates that the moon is a good platform for planetary radio astronomy observations. The noise level in the farside is quiet enough for observations of weak planetary radio waves. Because there is no dense ionosphere, planetary radio waves even in the low-frequency range can be observed from the moon's surface, where antenna arrays with rigid baselines will also be available in the future.

6.3 Artificial Radio Waves from the Earth's Radio Stations

In the summary plot of LRS radio wave observations shown in Fig. 21, we can find several banded emissions in a frequency around 3.9 MHz, 7.2 MHz, 9.6 MHz, 11.7 MHz, 13.7 MHz,

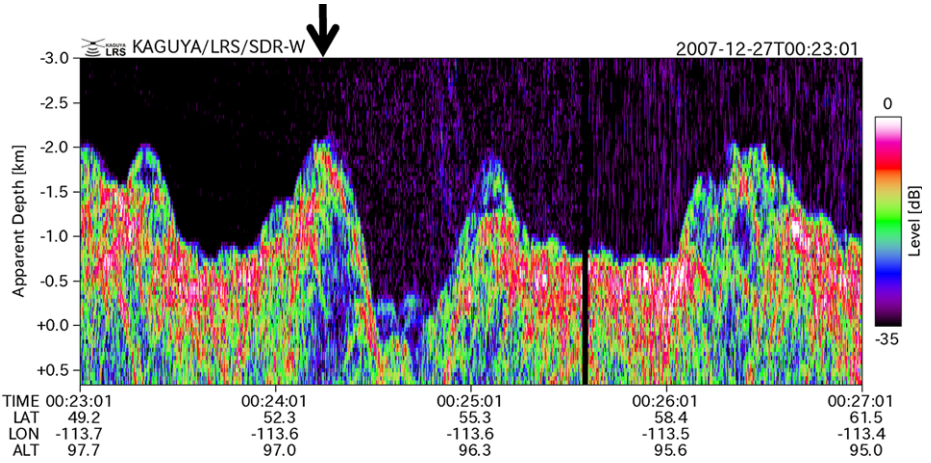

Fig. 25 Radargram interfered by the artificial radio waves from the Earth. The noise level before the surface echo arrives increases from 00:24:15 (indicated by *arrow*) when the Earth becomes visible from the spacecraft

and 14.8 MHz. They are artificial radio waves from the Earth's radio stations for broadcasting and telecommunication. The artificial radio waves interfered not only with the natural radio and plasma wave observations but also with radar sounding observation. Figure 25 shows an example of a radargram that was interfered with artificial radio waves from the Earth. The noise level before the surface echo arrives increases just when the Earth becomes visible from the spacecraft.

Figure 21 also shows that the intensities of the artificial radio waves in a frequency range from 3 MHz to 12 MHz simultaneously decrease every month as indicated by the white arrows. The timing of attenuation coincides with the moon moving in the dayside of the Earth, which suggests that the Earth's dayside ionosphere shields the artificial radio waves from the ground stations. Disappearance of AKR apparently coincides with attenuations of artificial radio waves. The disappearance of AKR is however caused by quite different mechanisms as described in Sect. 6.1. The AKR sources are located above the Earth's ionosphere. It can not be shielded by the Earth's dayside ionosphere.

Figure 26 shows the background noise levels in the farside and nearside of the moon. The noise level is quite low in the farside because the radio waves from the Earth cannot reach the farside of the moon. The background noise level in the nearside of the moon shows dependence on the sunlit condition of the Earth's ionosphere. When the moon is in the dayside of the Earth, broadcast radio waves are seen only in a frequency above 10 MHz. When the moon is in the nightside of the Earth, the broadcast radio waves were observed in wide frequency range. The longitudinal dependence of the artificial radio waves was also found in Fig. 26. The main peak of the artificial radio waves is at longitude around 90°E and sub-peak is at longitude around 40°W. Kaiser et al. (1996) reported that artificial radio waves from the Earth were detected by WIND spacecraft. They also pointed out that artificial radio waves are especially intense in the Indian sector.

The observation of terrestrial noises clearly shows that the farside of the moon can be a noise-free region for planetary radio astronomy observations as also mentioned in Sect. 6.2. However it should be noted that suppression of spacecraft noises, as unfortunately seen around 1 and 2 MHz in the LRS case, will be important in order to utilize the farside of the moon as a noise-free circumstance.

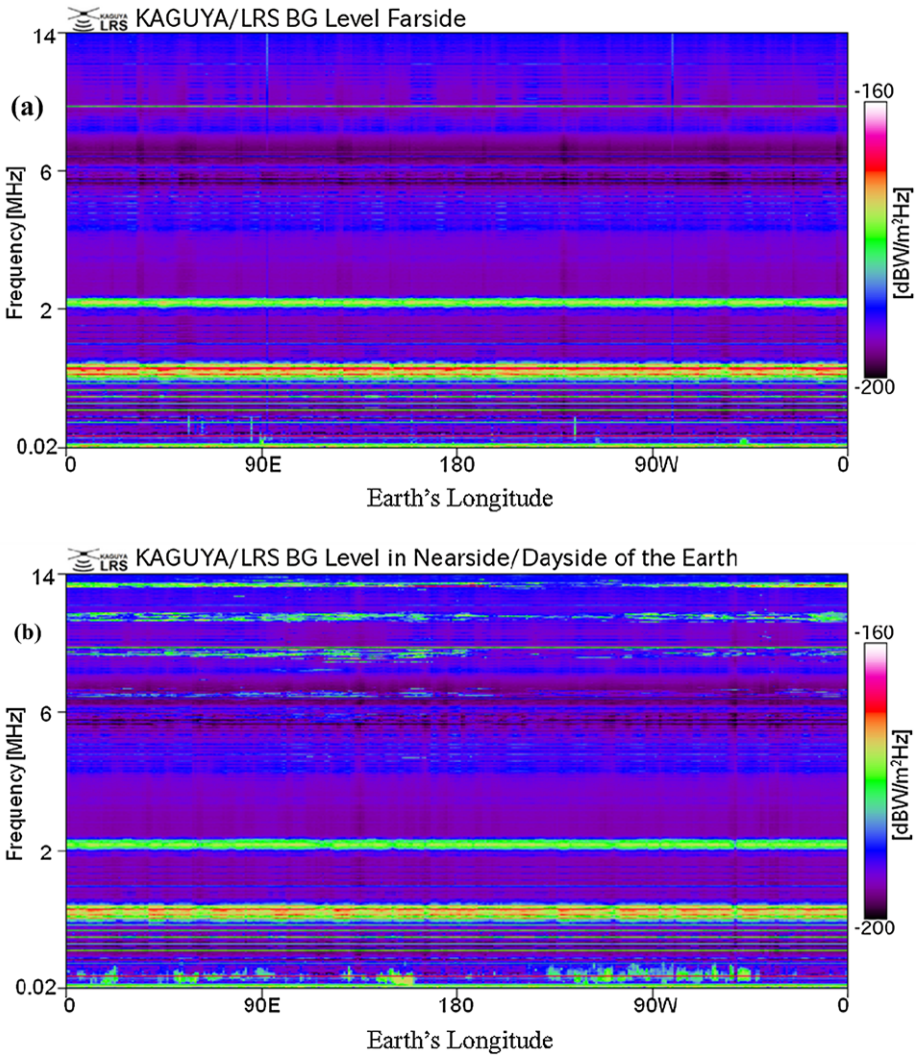

Fig. 26 Background noise levels (**a**) in the farside of the moon, (**b**) in the nearside of the moon and dayside of the Earth, and (**c**) in the nearside of the moon and nightside of the Earth. Horizontal axis indicates Earth's longitude of KAGUYA, and vertical axis indicates frequency. The broadcast radio waves from the Earth are detected in the nearside of the moon. The intensity also depends on the sunlit conditions of the Earth's ionosphere

7 Initial Results of Plasma and Radio Wave Observations Below 1 MHz

7.1 Spectrogram and Waveforms Obtained by the WFC Receiver in the Solar Wind

Figure 27 shows an example of the WFC-H spectrogram. The vertical axis is given in frequency from 1 kHz to 1 MHz, and the horizontal axis is given in time from 22:00 UT on October 30 to 00:00 UT on October 31, 2007. Note that the line noise at 200 kHz is an artificial noise caused by the ECU. In this period, the moon was in the solar wind and several

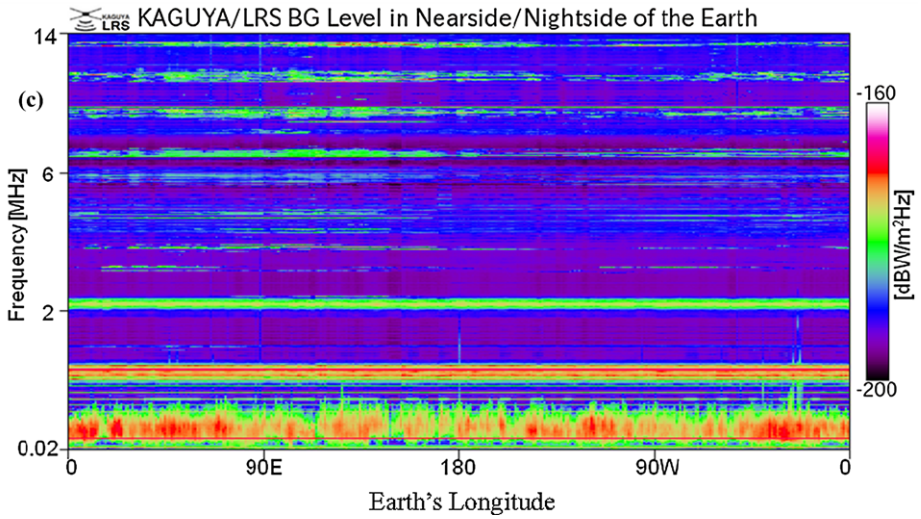

Fig. 26 (*Continued*)

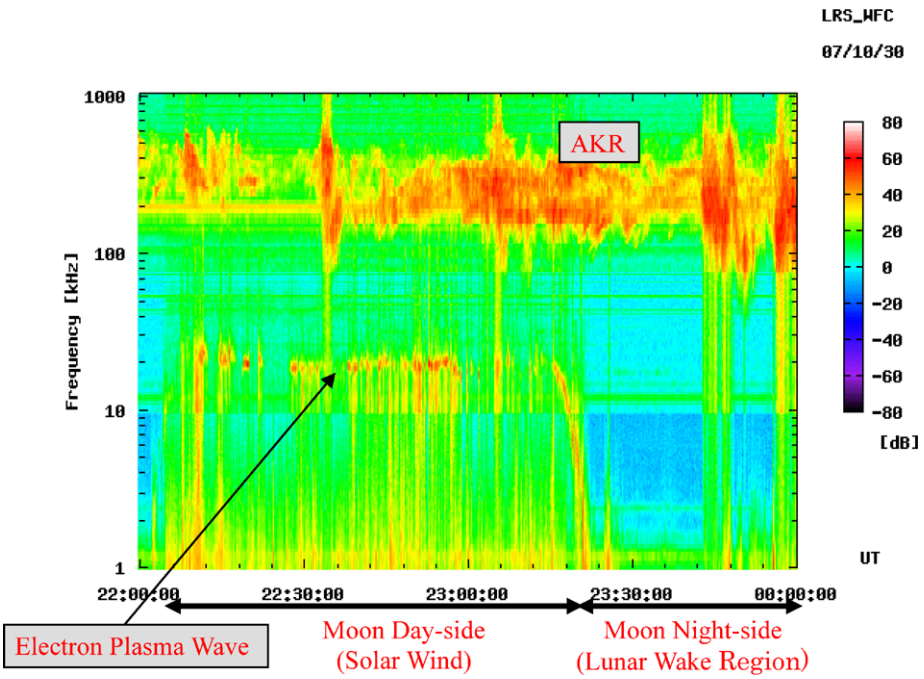

Fig. 27 A spectrogram observed from 22:00 UT on October 30 to 00:00 UT on October 31, 2007 by the WFC-H

kinds of natural plasma waves were observed. KAGUYA was designed to go around the moon passing over the lunar north pole and south pole every 2 hours with an inclination of 90 degrees, and it was located in the dayside region from 22:05 UT to 23:18 UT, and in the nightside region during the other time periods.

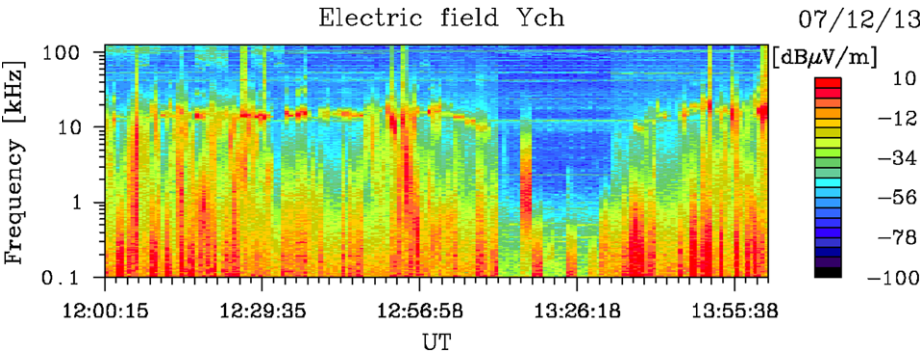

Fig. 28 A spectrogram of the WFC-L from 12:00 UT to 14:00 UT on December 13

In the higher frequency range from 70 kHz to 600 kHz, intense AKR was observed. From 22:05 UT to 23:15, when KAGUYA was located at the moon dayside, an intense wave around 20 kHz was observed. This wave was constantly observed in the frequency range of 10–20 kHz in the sunlit region, while the frequency suddenly decreased in the edge of the shade (occultation) region. This feature is quite similar to the observations by WIND when WIND crossed the lunar wake at a distance of $\sim 6.8 R_L$ (Kellogg et al. 1996). This wave is assumed to be an electrostatic electron plasma wave enhanced at local plasma frequency (f_p).

It was also found that the wave activities were rather high in the moon dayside while it became quiet in the shade (lunar wake) region. This result suggests that the plasma environment in the dayside of the moon is quite complex due to interaction between solar wind and lunar body, while plasma density is rather low in the lunar wake although ions were unexpectedly observed even in the central part of the lunar wake (Nishino et al. 2009).

Figure 28 shows an example of WFC-L spectrogram from 12:00 UT to 14:00 UT on December 13, 2007. This spectrogram was given by processing the FFT analysis on the ground. Note that original waveforms were intermittently acquired with a duration of 1.5 sec almost every 2 minutes, and the spectrogram in Fig. 28 was made by joining each intermittent spectrum filling the time gap. Electron plasma waves around 15 kHz and broadband noise below several kHz were observed in the moon dayside region (from 12:00 to 13:14 UT, and from 13:38 to 14:00 UT).

When we examine broadband noise in more detail, it is found that a portion of broadband noise consists of bipolar pulses. Figure 29 shows an example of waveforms while KAGUYA was orbiting around the terminator of the moon at 13:00:46 UT on July 10, 2008. The WFC-L captured two orthogonal differential signals with a sampling frequency of 250 kHz. A pair of waveforms measured in X and Y components were indicated with a total time interval of 40 msec. Several bipolar pulses were observed both in X and Y components and these waves could be broadband noise below several kHz. The bipolar pulses shown in Fig. 29 are considered to be electrostatic solitary waves (ESW). According to the observation by the WFC-L, ESW were frequently observed around the moon in the solar wind and also lunar wake boundary (Hashimoto et al. 2010). However we also find other types of broadband noises which cannot be interpreted as ESW and more detailed waveform analyses including generation mechanism and statistical study will be needed for the future work.

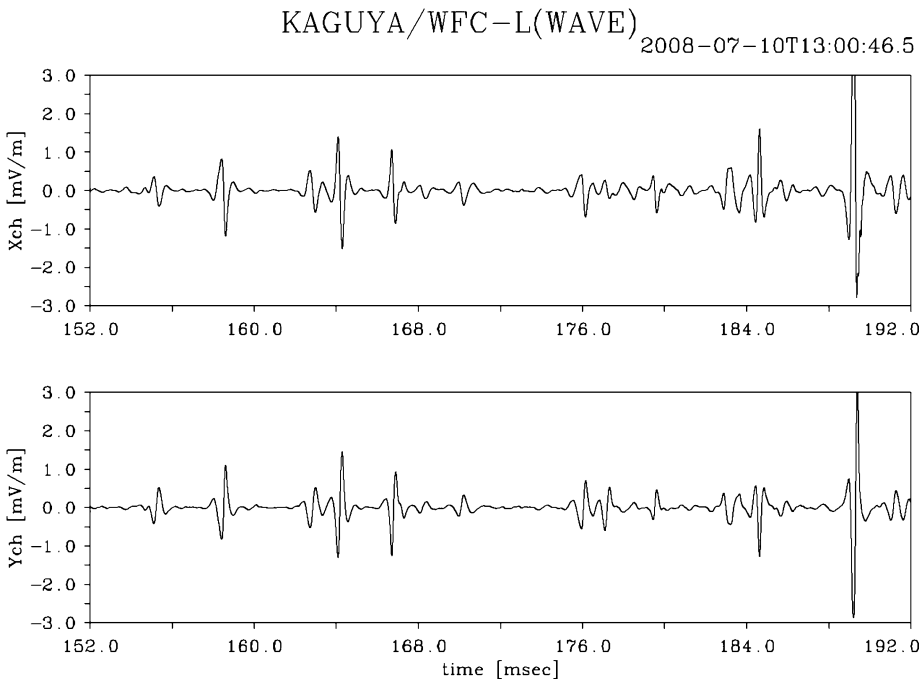

Fig. 29 An example of electrostatic solitary waves observed at 13:00:46 UT on July 10, 2008

7.2 Electron Density Profile in the Lunar Wake

Local plasma density can be derived tracing local f_p from the WFC-H spectrum along the trajectory of KAGUYA. Figure 30 is a typical example of the electron density profile measured on December 13, 2007. The upper panel shows the dynamic spectrum of the WFC-H-Y component and the second panel shows the electron density derived from the frequency of electron plasma wave enhanced at local f_p. The third panel shows the eclipse rate of the sun at the observation point. The 1st and 3rd panels at the bottom show the locations of the Earth and the moon in the GSE (Geocentric Solar Ecliptic) X-Z and X-Y planes, respectively. The moon was in the solar wind, as shown by these panels. The 2nd and 4th panels at the bottom show the trajectory of KAGUYA around the moon. Green circles show the trajectory of KAGUYA. Red arrows in these panels indicate the direction of the Earth. Electron density was 2∼3/cc in the solar wind and it suddenly decreased down to 0.5/cc in the boundary region of lunar wake. It was unable to detect electron density in the lunar wake because wave activity was too quiet to trace local f_p.

In general, electron parameters such as electron density and temperature can be derived from the particle detector. Halekas et al. (2005) made a statistical study on the lunar wake structure using the Magnetometer (MAG) and Electron Reflectometer (ER) onboard Lunar Prospector (LP). They showed that wake signature at an altitude range of 85–115 km was classical while they observed an ambipolar potential drop across the wake boundary and greatly reduced electron density and increased electron temperature in the wake at 20–45 km. However, the electron density derived from the ER was an approximation because the lowest energy range of the ER was ∼40 eV and it did not allow for accurate direct integration of the energy distribution of electron (Halekas et al. 2005). On the other hand, our measurement uses a direct method to determine local f_p and thus we expect that absolute

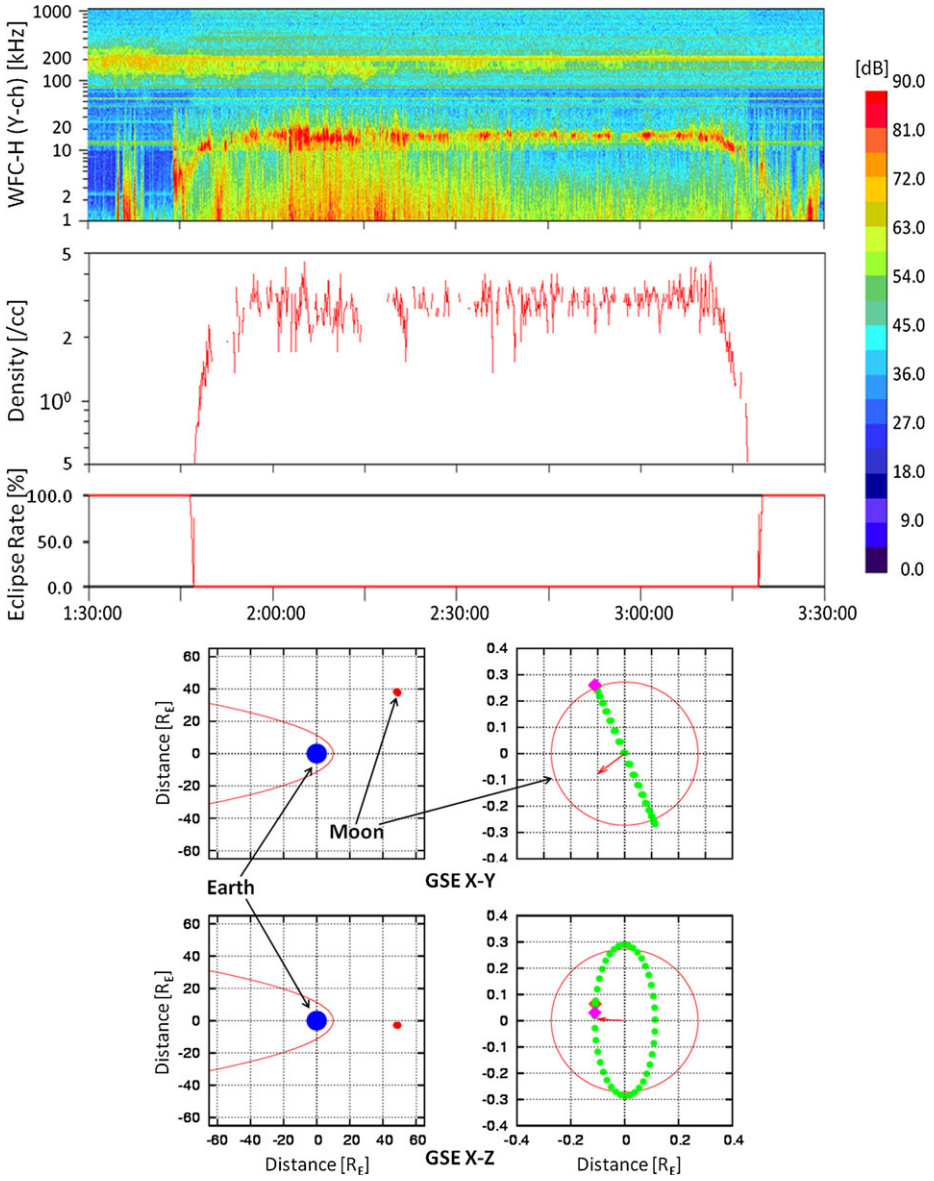

Fig. 30 An example of electron profile derived from a WFC-H spectrogram. The *upper panel* shows the dynamic spectrum of the WFC-H and the *second panel* shows the electron density profile along the trajectory. The *third panel* shows eclipse rate of the sun at the observation point. The *1st* and *3rd panels at the bottom* show the locations of the Earth and the moon in the GSE X-Z and X-Y planes, respectively. The *2nd* and *4th panels at the bottom* show the trajectory of KAGUYA around the moon. *Green circles* show the trajectory of KAGUYA. Red arrows in these panels indicate the direction of the Earth

density can be derived. While WIND crossed the lunar wake and local f_p falling and rising in frequency at the lunar wake boundary was detected at a distance of $\sim 6.8 R_L$ (Kellogg et al. 1996), KAGUYA experienced encounters with the lunar wake every 2 hours in a re-

gion much closer to the moon. Varieties of frequency transition of f_p were recognized by the WFC-H through the nominal mission as well as the extended mission depending on the orbital condition of KAGUYA. Statistical analysis of electron density profile is now under study but it is expected to derive global electron density profile around the moon including the spatial structure of the lunar wake boundary region.

8 Summary

The LRS onboard the KAGUYA spacecraft has successfully performed radar sounder observations of the lunar subsurface structures and passive observations of natural radio and plasma waves in the lunar orbit. Through the operation, from October 29, 2007 to June 10, 2009, 2363 hours worth of radar sounder data and 8961 hours worth of wave data have been obtained.

KAGUYA/LRS has successfully performed global radar sounder observations of the moon. The observations revealed that there are subsurface reflectors with depths of several hundred meters in several nearside maria. The reflectors are inferred to be buried regolith covered by basalt lava flows. The subsurface structure below the mare ridge in the Mare Serenitatis suggests that constructing stress occurred after 2.84 billion years ago. It was also suggested that echo power loss by surface material such as TiO_2 should be taken into account when we investigate radargrams obtained at the moon. As shown by the above results, the datasets have enough potential to make contributions for studies on the lunar geology associated with the origin and evolution of the moon.

The passive measurements by the LRS using the NPW and WFC subsystems have revealed many interesting wave phenomena which were locally generated as well as radio emissions propagating from far source regions. The operation was successfully performed and it was demonstrated that we could obtain so much data closely related to the plasma physics around the moon. It is indispensable to perform collaborative studies with magnetic field and particle data in the near future for further investigation. The background noise level data measured by the LRS will be useful in planning future projects of low-frequency radio telescope stations on the moon.

Since November 2009, the KAGUYA/LRS Level-2 data have been open to researchers interested in lunar subsurface radar soundings and natural radio and plasma wave observations. We hope that further studies on the lunar geology and physics of natural radio and plasma waves are performed with datasets obtained by KAGUYA/LRS.

Acknowledgements The KAGUYA mission was conducted by the Japan Aerospace Exploration Agency (JAXA). The authors thank Y. Takizawa, S. Sasaki, and M. Kato for their efforts in accomplishing the KAGUYA mission, and K. Tanaka, Y. Iijima, S. Nakazawa, H. Ohtake, S. Sobue, H. Hoshino, H. Okumura, Y. Yamamoto, and J. Kimura for their helpful discussions on achieving a high reliability for the mission instruments. The authors express their deep appreciation to Drs. H. Kojima and Y. Ueda and to Mr. H. Iwai for their valuable suggestions and discussions on the development of the onboard software of WFC. The authors are also grateful to Professors I. Nagano, T. Okada, M. Tsutsui, Y. Kasaba, and S. Yagitani, and Dr. K. Ishisaka for their helpful suggestions and contribution to the hardware design and the development of the WFC. The authors thank Mr. A. Muro and Mr. Horie for their help in the evaluation of the data quality of the WFC and preparation of the part of figures in the paper.

References

Analog Devices Inc., AD9260 High-Speed Oversampling CMOS ADC with 16-Bit Resolution at a 2.5 MHz Output Word Rate (AD9260 Data Sheet, 2004). http://www.analog.com/static/imported-files/data_sheets/AD9260.pdf. Accessed 21 February 2010

H. Araki, S. Tazawa, H. Noda, T. Tsubokawa, N. Kawano, S. Sasaki, Adv. Space Res. **42**, 317–322 (2008). doi:10.1016/j.asr.2007.05.042
H. Araki, S. Tazawa, H. Noda, Y. Ishihara, S. Gossens, S. Sasaki, N. Kawano, I. Kamiya, H. Otake, J. Oberst, C. Shum, Science **323**, 897–900 (2009). doi:10.1126/science.1164146
J.-L. Bougeret, Adv. Space Res. **18**(11), 35–41 (1996). doi:10.1016/0273-1177(96)00085-3
J.-L. Bougeret, M.L. Kaiser, P.J. Kellogg, R. Manning, K. Goetz, S.J. Monson, N. Monge, L. Friel, C.A. Meetre, C. Perche, L. Sitruk, S. Hoang, Space Sci. Rev. **71**(1–4), 231–263 (1995). doi:10.1007/BF00751331
J.-L. Bougeret, K. Goetz, M.L. Kaiser, S.D. Bale, P.J. Kellogg, M. Maksimovic, N. Monge, S.J. Monson, P.L. Astier, S. Davy, M. Dekkali, J.J. Hinze, R.E. Manning, E. Aguilar-Rodriguez, X. Bonnin, C. Briand, I.H. Cairns, C.A. Cattell, B. Cecconi, J. Eastwood, R.E. Ergun, J. Fainberg, S. Hoang, K.E.J. Huttunen, S. Krucker, A. Lecacheux, R.J. MacDowall, W. Macher, A. Mangeney, C.A. Meetre, X. Moussas, Q.N. Nguyen, T.H. Oswald, M. Pulupa, M.J. Reiner, P.A. Robinson, H. Rucker, C. Salem, O. Santolik, J.M. Silvis, R. Ullrich, P. Zarka, I. Zouganelis, Space Sci. Rev. **114**, 395–463 (2004)
T.D. Carr, M.D. Desch, in *Jupiter*, ed. by T. Gehrels (University of Arizona Press, Tucson, 1976), p. 693
B.L. Cooper, J.L. Carter, C.A. Sapp, J. Geophys. Res. **99**(E2), 3799–3812 (1994)
R.A. DeHon, J.D. Waskom, in *Proc. Lunar Sci. Conf. 7th* (1976), pp. 2729–2746
G.A. Dulk, W.C. Erickson, R. Manning, J.-L. Bougeret, Astron. Astrophys. **365**, 294–300 (2001)
W.M. Farrell, R.J. Fitzenreiter, C.J. Owen, J.B. Byrnes, R.P. Lepping, K.W. Ogilvie, F. Neubauer, Geophys. Res. Lett. **23**, 1271–1274 (1996)
W.M. Farrell, M.L. Kaiser, J.T. Steinberg, Geophys. Res. Lett. **24**, 1135–1138 (1997)
C.A. Franklin, M.A. MacLean, Proc. IEEE **57**, 897–929 (1969)
F. Genova, A. Boischot, Nature **293**, 382–383 (1981). doi:10.1038/293382a0
F. Genova, Y. Leblanc, Astron. Astrophys. **98**, 133–139 (1981)
Y. Goto, T. Fujimoto, Y. Kasahara, A. Kumamoto, T. Ono, Earth Planets Space (2009). doi:10.1029/JA082i013p01825
J.L. Green, D.A. Gurnett, S.D. Shawhan, J. Geophys. Res. **82**, 1825 (1977)
D.A. Gurnett, J. Geophys. Res. **79**, 4227–4238 (1974)
D.A. Gurnett, W.S. Kurth, D.L. Kirchner, G.B. Hospodarsky, T.F. Averkamp, P. Zarka, A. Lecacheux, R. Manning, A. Roux, P. Canu, N. Cornilleau-Wehrlin, P. Galopeau, A. Meyer, R. Bostrom, G. Gustafsson, J.-E. Wahlund, L. Aahlen, H.O. Rucker, H.P. Ladreiter, W. Macher, L.J.C. Woolliscroft, H. Alleyne, M.L. Kaiser, M.D. Desch, W.M. Farrell, C.C. Harvey, P. Louarn, P.J. Kellogg, K. Goetz, A. Pedersen, Space Sci. Rev. **114**, 395–463 (2004)
D.A. Gurnett, D.L. Kirchner, R.L. Huff, D.D. Morgan, A.M. Persoon, T.F. Averkamp, F. Duru, E. Nielsen, A. Safaeinili, J.J. Plaut, G. Picardi, Science **310**, 1929–1933 (2005). doi:10.1126/science.1121868
J.S. Halekas, S.D. Bale, D.L. Mitchell, R.P. Lin, J. Geophys. Res. **110**, A07222 (2005). doi:10.1029/2004JA010991
J. Haruyama, T. Matsunaga, M. Ohtake, T. Morota, Y. Yokota, C. Honda, M. Torii, Y. Ogawa (LISM Working Group), Earth Planets Space **60**, 243–256 (2008)
K. Hashimoto, H. Iwai, Y. Ueda, H. Kojima, H. Matsumoto, IEEE Trans. Geosci. Remote Sens. **41**(11), 2638–2647 (2003)
K. Hashimoto, M. Hashitani, Y. Kasahara, Y. Omura, M.N. Nishino, Y. Saito, S. Yokota, T. Ono, H. Tsunakawa, H. Shibuya, M. Matsushima, H. Shimizu, F. Takahashi, Geophys. Res. Lett. (2010, in press)
H. Hieginger, R. Jaumann, G. Neukum, J.W. Head III, J. Geophys. Res. **105**(E12), 29,239–29,275 (2000)
H. Hieginger, J.W. Head III, U. Wolf, R. Jaumann, G. Neukum, J. Geophys. Res. **108**(E7), 5065 (2003). doi:10.1029/2002JE001985
M. Imai, K. Imai, C.A. Higgins, J.R. Thieman, Geophys. Res. Lett. **35**, L17103 (2008). doi:10.1029/s2008GL034987
T. Imamura, K. Oyama, T. Iwata, Y. Kono, K. Matsumoto, Q. Liu, H. Noda, Y. Futaana, A. Nabatov, Earth Planets Space **60**, 387–390 (2008)
Intersil Corporation, HSP50214B Programmable Down Converter (HSP50214B Data Sheet, 2007). http://www.intersil.com/data/fn/fn4450.pdf. Accessed 21 February 2010
J.E. Jackson, E.S. Warren, Proc. IEEE **57**, 861–865 (1969)
H.G. James, E.L. Hagg, D.L.P. Strange, in *AGARD Conf. Proc.*, AGARD-CP-138, 24-1-7 (1974)
R. Jordan, G. Picardi, J. Plaut, K. Wheeler, D. Kirchner, A. Safaeinili, W. Johnson, R. Seu, D. Calabrese, E. Zampolini, A. Cicchetti, R. Huff, D. Gurnett, A. Ivanov, W. Kofman, R. Orosei, T. Thompson, P. Edenhofer, O. Bombaci, Planet. Space Sci. **57**, 1975–1986 (2009). doi:10.1016/j.pss.2009.09.016
M.L. Kaiser, M.D. Desch, A.C. Riddle, A. Lecacheux, J.B. Pearce, J.K. Alexander, J.W. Warwick, J.R. Thieman, Geophys. Res. Lett. **6**, 507–510 (1979)
M.L. Kaiser, M.D. Desch, J.L. Bougeret, R. Manning, C.A. Meetre, Geophys. Res. Lett. **23**, 1287–1290 (1996)

Y. Kasahara, Y. Goto, K. Hashimoto, T. Imachi, A. Kumamoto, T. Ono, H. Matsumoto, Earth Planets Space **60**, 341–351 (2008)
M. Kato, S. Sasaki, K. Tanaka, Y. Iijima, Y. Takizawa, Adv. Space Res. **42**, 294–300 (2008)
P.J. Kellogg, K. Goetz, S.J. Monson, Geophys. Res. Lett. **23**, 1267–1270 (1996)
T. Kobayashi, H. Oya, T. Ono, Earth Planets Space **54**, 973–982 (2002a)
T. Kobayashi, H. Oya, T. Ono, Earth Planets Space **54**, 983–991 (2002b)
T. Kobayashi, T. Ono, J. Geophys. Res. **111**, E06S10 (2006). doi:10.1029/2005JE002575
T. Kobayashi, T. Ono, J. Geophys. Res. **112**, E03S90 (2007). doi:10.1029/2005JE002576
A. Kumamoto, T. Ono, Y. Kasahara, Y. Goto, Y. Iijima, S. Nakazawa, Earth Planets Space **60**, 333–340 (2008)
Z. Kuncic, I.H. Cairns, Geophys. Res. Lett. **31**, L11809 (2004). doi:10.1029/2004GL020008
M. Kurata, H. Tsunakawa, Y. Saito, H. Shibuya, M. Matsushima, H. Shimizu, Geophys. Res. Lett. **32**, L24205 (2005). doi:10.1029/2005GL024097
J. LaBelle, R.A. Treumann, M.H. Boehm, K. Gewecke, Radio Sci. **24**, 725–737 (1987)
A. Lecacheux, Adv. Space Res. **14**(6), 193–200 (1994). doi:10.1016/0273-1177(94)90027-2
R.P. Lin, D.L. Mitchell, D.W. Curtis, K.A. Anderson, C.W. Carlson, J. McFadden, M.H. Acuña, L.L. Hood, A. Binder, Science **281**, 1480–1484 (1998)
H. Matsumoto, I. Nagano, R.R. Anderson, H. Kojima, K. Hashimoto, M. Tsutsui, T. Okada, I. Kimura, Y. Omura, M. Okada, J. Geomagn. Geoelectr. **46**, 59–95 (1994a)
H. Matsumoto, H. Kojima, T. Miyatake, Y. Omura, M. Okada, I. Nagano, M. Tsutsui, Geophys. Res. Lett. **21**, 2915–2918 (1994b)
S.M. Milkovich, J.J. Plaut, J. Geophys. Res. **113**, E06007 (2008). doi:10.1029/2007JE002987
S.M. Milkovich, J.J. Plaut, A. Safaeinili, G. Picardi, R. Seu, R.J. Phillips, J. Geophys. Res. **114**, E03002 (2009). doi:10.1029/2008JE003162
T. Nakagawa, Y. Takahashi, M. Iizima, Earth Planets Space **55**, 569–580 (2003)
N.F. Ness, K.W. Behannon, H.E. Taylor, Y.C. Whang, J. Geophys. Res. **73**, 3421–3440 (1968)
M.N. Nishino, M. Fujimoto, K. Maezawa, Y. Saito, S. Yokota, K. Asamura, T. Tanaka, H. Tsunakawa, M. Matsushima, F. Takahashi, T. Terasawa, H. Shibuya, H. Shimizu, Geophys. Res. Lett. **36**, L16103 (2009). doi:10.1029/2009GL039444
T. Obara, H. Oya, J. Geomagn. Geoelectr. **37**, 285–307 (1985)
G.R. Olhoeft, D.W. Strangway, Earth Planet. Sci. Lett. **24**, 394–404 (1975)
T. Ono, H. Oya, Earth Planets Space **52**, 629–637 (2000)
T. Ono, H. Oya, A. Morioka, A. Kumamoto, K. Kobayashi, T. Obara, T. Nakagawa, Earth Planets Space **50**, 213–221 (1998)
T. Ono, A. Kumamoto, Y. Yamaguchi, A. Yamaji, T. Kobayashi, Y. Kasahara, H. Oya, Earth Planets Space **60**, 321–332 (2008)
T. Ono, A. Kumamoto, H. Nakagawa, Y. Yamaguchi, S. Oshigami, A. Yamaji, T. Kobayashi, Y. Kasahara, H. Oya, Science **323**, 909–912 (2009)
S. Oshigami, Y. Yamaguchi, A. Yamaji, T. Ono, A. Kumamoto, T. Kobayashi, H. Nakagawa, Geophys. Res. Lett. **36**, L18202 (2009). doi:10.1029/2009GL039835
H. Oya, T. Ono, Adv. Space Res. **1**, 217–220 (1981)
H. Oya, T. Ono, J. Geomagn. Geoelectr. **39**, 591–607 (1987)
H. Oya, T. Ono, Earth Planets Space **50**, 229–234 (1998)
H. Oya, T. Ono, T. Kamada, J. Geomagn. Geoelectr. **33**(1), 3–25 (1981)
H. Oya, A. Morioka, T. Obara, J. Geomagn. Geoelectr. **37**, 237–262 (1985)
H. Oya, A. Morioka, K. Kobayashi, M. Iizima, T. Ono, H. Miyaoka, T. Okada, T. Obara, J. Geomagn. Geoelectr. **42**, 411–442 (1990)
W.J. Peeples, W.R. Sill, T.W. May, S.H. Ward, R.J. Phillips, R.L. Jordan, E.A. Abbott, T.J. Killpack, J. Geophys. Res. **83**(B7), 3459–3468 (1978). doi:10.1029/JB083iB07p03459
R.J. Phillips, G.F. Adams, W.E. Brown Jr., R.E. Eggleton, P.L. Jackson, R. Jordan, W.I. Linlor, W.J. Peeples, L.J. Porcello, J. Ryu, G. Schaber, W.R. Sill, T.W. Thompson, S.H. Ward, J.S. Zelenka, NASA Spec. Publ. **330**(22), 1–26 (1973)
G. Picardi, D. Biccari, R. Seu, J. Plaut, W.T.K. Johnson, R.L. Jordan, A. Safaeinili, D.A. Gurnett, R. Huff, R. Orosei, O. Bombaci, D. Calabrese, E. Zampolini, in *Mars Express: A European Mission to the Red Planet*. Eur. Space Agency Spec. Publ., ESA SP-1240 (2004), pp. 51–69
G. Picardi, J.J. Plaut, D. Biccari, O. Bombaci, D. Calabrese, M. Cartacci, A. Cicchetti, S.M. Clifford, P. Edenhofer, W.M. Farrell, C. Federico, A. Frigeri, D.A. Gurnett, T. Hagfors, E. Heggy, A. Herique, R.L. Huff, A.B. Ivanov, W.T.K. Johnson, R.L. Jordan, D.L. Kirchner, W. Kofman, C.J. Leuschen, E. Nielsen, R. Orosei, E. Pettinelli, R.J. Phillips, D. Plettemeier, A. Safaeinili, R. Seu, E.R. Stofan, G. Vannaroni, T.R. Watters, E. Zampolini, Science **310**(5756), 1925–1928 (2005). doi:10.1126/science.1122165
R.J. Pike, Geophys. Res. Lett. **1**, 291–294 (1974). doi:10.1029/GL001i007p00291

J.J. Plaut, G. Picardi, A. Safaeinili, A.B. Ivanov, S.M. Milkovich, A. Cicchetti, W. Kofman, J. Mouginot, W.M. Farrell, R.J. Phillips, S.M. Clifford, A. Frigeri, R. Orosei, C. Federico, I.P. Williams, D.A. Gurnett, E. Nielsen, T. Hagfors, E. Heggy, E.R. Stofan, D. Plettemeier, T.R. Watters, C.J. Leuschen, P. Edenhofer, Science **316**, 92–95 (2007). doi:10.1126/science.1139672

A. Pommerol, W. Kofman, J. Audouard, C. Grima, P. Beck, J. Mouginot, A. Herique, A. Kumamoto, T. Kobayashi, T. Ono, Geophys. Res. Lett. **37**, L03201 (2010). doi:10.1029/2009GL041681

L.J. Porcello, R.L. Jordan, J.S. Zelenka, G.F. Adams, R.J. Phillips, W.E. Brown Jr., S.H. Ward, P.L. Jackson, Proc. IEEE **62**, 769–783 (1974)

U. Samir, K.H. Wright Jr., N.H. Stone, Rev. Geophys. Space Phys. **21**, 1631–1646 (1983)

M. Schindler, Range Encoder Homepage (Data Compression Consulting Webpage, 1999). http://www.compressconsult.com/rangecoder/. Accessed 21 February 2010

G. Schubert, B.R. Lichtenstein, Rev. Geophys. Space Phys. **12**, 592–626 (1974)

R. Seu, D. Biccari, R. Orosei, L.V. Lorenzoni, R.J. Phillips, L. Marinangeli, G. Picardi, A. Masdea, E. Zampolini, Planet. Space Sci. **52**(1–3), 157–166 (2004)

R. Seu, R.J. Phillips, D. Biccari, R. Orosei, A. Masdea, G. Picardi, A. Safaeinili, B.A. Campbell, J.J. Plaut, L. Marinangeli, S.E. Smrekar, D.C. Nunes, J. Geophys. Res. **112**, E05S05 (2007). doi:10.1029/2006JE002745

V.L. Sharpton, J.W. Head III, J. Geophys. Res. **87**(B13), 10983–10998 (1982)

S.C. Solomon, J.W. Head, Rev. Geophys. Space Phys. **18**, 107–141 (1980)

A.S. Vyshlov, N.A. Savich, Cosm. Res. **16**, 450–454 (1979)

T.R. Watters, C.J. Leuschen, J.J. Plaut, G. Picardi, A. Safaeinili, S.M. Clifford, W.M. Farrell, A.B. Ivanov, R.J. Phillips, E.R. Stofan, Nature **444**, 905–908 (2006). doi:10.1038/nature05356

J.P. Wild, L.L. McCready, Aust. J. Sci. Res. Ser. A **3**, 387–397 (1950)

J.P. Wild, J.A. Roberts, J.D. Murray, Nature **173**, 532–534 (1954). doi:10.1038/173532a0

K.K. Williams, M.T. Zuber, Icarus **131**, 107–122 (1998). doi:10.1006/icar.1997.5856

A. Yamaji, S. Sasaki, Y. Yamaguchi, T. Ono, J. Haruyama, T. Okada, Mem. Geol. Soc. Jpn. **50**, 213–226 (1998)